



저작자표시-비영리-변경금지 2.0 대한민국

이용자는 아래의 조건을 따르는 경우에 한하여 자유롭게

- 이 저작물을 복제, 배포, 전송, 전시, 공연 및 방송할 수 있습니다.

다음과 같은 조건을 따라야 합니다:



저작자표시. 귀하는 원저작자를 표시하여야 합니다.



비영리. 귀하는 이 저작물을 영리 목적으로 이용할 수 없습니다.



변경금지. 귀하는 이 저작물을 개작, 변형 또는 가공할 수 없습니다.

- 귀하는, 이 저작물의 재이용이나 배포의 경우, 이 저작물에 적용된 이용허락조건을 명확하게 나타내어야 합니다.
- 저작권자로부터 별도의 허가를 받으면 이러한 조건들은 적용되지 않습니다.

저작권법에 따른 이용자의 권리는 위의 내용에 의하여 영향을 받지 않습니다.

이것은 [이용허락규약\(Legal Code\)](#)을 이해하기 쉽게 요약한 것입니다.

[Disclaimer](#)

Master's Thesis

**Multiple Reconfigurable Intelligent Surfaces for
Improving Performance of Multiple Antenna
Wireless Communication Networks**

Nguyen Khac Tuan

Department of
Electrical, Electronic and Computer Engineering

University of Ulsan

2023

Multiple Reconfigurable Intelligent Surfaces for Improving Performance of Multiple Antenna Wireless Communication Networks

A Thesis Submitted in Partial Fulfilment of the Requirements
for the Degree of

MASTER OF SCIENCE

by

Nguyen Khac Tuan

Department of
Electrical, Electronic and Computer Engineering
University of Ulsan

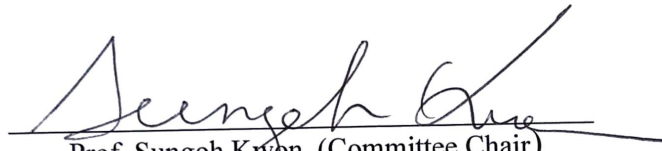
July 2023

VITA


Khac-Tuan Nguyen received his B.S. degree from the Post and Telecommunications Institute of Technology, Vietnam, in 2021. He is currently pursuing the M.S. degree with the School of Electrical Engineering, University of Ulsan, South Korea. His research interests include future wireless communication and deep/machine learning for wireless communication.

Multiple Reconfigurable Intelligent Surfaces for Improving Performance of Multiple Antenna Wireless Communication Networks

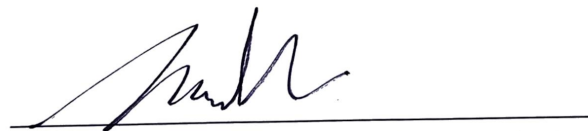
The thesis of Nguyen Khac Tuan is approved.



Prof. Sungoh Kwon, (Committee Chair)



Prof. Hee-Youl Kwak, (Committee Member)



Prof. Sunghwan Kim, (Committee Member)

July 2023

ACKNOWLEDGEMENT

I would like to express my heartfelt gratitude to my supervisor, Professor Sunghwan Kim, for his unwavering support, guidance, and encouragement throughout my research. His insightful feedback and constructive criticism were instrumental in shaping the direction of my work, and I could not have accomplished this without his constant motivation and inspiration.

I would also like to thank my labmates, friends, and family for their love and encouragement, which provided me with the strength to persevere during challenging times. I am grateful to my parents for their unwavering support and belief in my abilities. Their sacrifices have enabled me to pursue my dreams and make it to this point.

Finally, I would like to express my gratitude to all the participants who generously gave their time and shared their experiences with me. Their willingness to participate in my research made it possible for me to complete my study successfully.

Once again, thank you to all those who have contributed to my master's thesis.

ABSTRACT

Multiple Reconfigurable Intelligent Surfaces for Improving Performance of Multiple Antenna Wireless Communication Networks

by

Nguyen Khac Tuan
Supervisor: Professor Sunghwan Kim

Submitted in Partial Fulfilment of the Requirements for the Degree of
Master of Science
July 2023

This thesis analyzes the performance of an uplink/downlink reconfigurable intelligent surface (RIS)-based wireless system with a multiple-antenna base station (B). The RIS selection strategy is considered to reduce overhead and optimize resources. To enhance system performance, the study investigates maximal-ratio-combining (MRC) and selection-combining (SC) for uplink transmission, and maximum-ratio-transmission (MRT) and beamforming for downlink transmission. The work proposes two methods of beamforming design: direct-path beamforming design (DBD) and reflective-path beamforming design (RBD). Additionally, the impacts of uncertain phase shift (UPS) and optimal phase shift (OPS) alignments were also studied. Closed-form expressions for each uplink and downlink scenario's outage probability (OP) are derived. The numerical results indicate that using MRC at the B and OPS at RIS in the uplink transmission yields the best performance. For small antenna settings, employing SC-enabled OPS outperforms MRC-integrated UPS. In the downlink transmission, RBD outperforms DBD, and MRT at the B and OPS at the RIS again provide superior performance over UPS.

Contents

List of Figures	vii
List of Tables	viii
1 Introduction	1
1.1 Reconfigurable Intelligent Surface	1
1.2 RIS in Wireless Communication	3
1.3 An Example	4
1.4 Organization	7
2 Performance Analysis of Multiple RIS-aided Wireless Communication Networks	8
2.1 Uplink System model	12
2.1.1 Channel Model Description	13
2.1.2 Outage Probability Analysis	15
2.2 Downlink System Model	23
2.2.1 Channel Model Description	23
2.2.2 Outage Probability Analysis	25
3 Results and Discussion	33
3.1 Uplink Model	34
3.2 Downlink Model	38
4 Conclusions	44
Bibliography	46

List of Figures

1.1	Structure and RIS operations relying on diodes.	2
1.2	RIS applications.	3
1.3	A single RIS-aided single-input single-output system.	4
1.4	A comparison of RIS and conventional systems.	6
2.1	Uplink model	12
2.2	Downlink model	23
3.1	Effects of N on the OP of B with $M = 5$ and $K = 30$	34
3.2	Effects of M on the OP of B with $N = 5$ and $K = 30$	36
3.3	Effects of the number of the reflector at RIS on the OP of B when $M = 6$ and $N = 4$	36
3.4	Effects of SNR (dB) on the OP of B with $M = 6$, $N = 4$, and $K =$ 30	37
3.5	Effects of N on the OP of U with $M = 5$ and $K = 30$	39
3.6	Effects of M on the OP of U with $N = 5$ and $K = 30$	40
3.7	Effects of the number of reflectors at RIS on the OP of U with M $= 6$ and $N = 4$	41
3.8	Effects of SNR (dB) on the OP of U with $M = 6$, $N = 4$, and $K =$ 30	42
3.9	The effects of the number of summation terms on closed-form ex- pressions with $M = 6$, $N = 4$, and $K = 30$	42

List of Tables

3.1	Parameters and values for analysis and simulation.	33
-----	--	----

Notations and Abbreviations

5G	fifth-generation
6G	sixth-generation
CDF	cumulative distribution function
CSI	channel state information
DBD	direct-path beamforming design
MISO	multiple-input single-output
MIMO	multiple-input multiple-output
MRC	maximal ratio combining
MRT	maximal ratio transmission
OPS	optimal phase shift
OP	outage probability
$\Pr(\cdot)$	probability
SC	selection combining
SISO	single-input single-output
SNR	signal-to-noise ratio
RBD	reflective-path beamforming design
RIS	Reconfigurable intelligent surfaces
Rx	receiver
Tx	transmitter
UPS	uncertain phase shift
$f_X(x)$	PDF of the random variable X
$F_X(x)$	CDF of the random variable X

Chapter 1

Introduction

1.1 Reconfigurable Intelligent Surface

Reconfigurable intelligent surfaces (RIS) are a new class of metasurfaces that are able to control the propagation of electromagnetic waves. RIS is composed of a large number of small passive elements that can be electronically tuned to modify the amplitude and phase of reflected or transmitted waves [22]. By changing the phase and amplitude of incident electromagnetic waves, RIS can create desirable patterns of reflected or transmitted waves, thus enabling a new degree of control over electromagnetic fields.

The key component of RIS is the passive element, which can be designed using a variety of techniques such as metamaterials, metasurfaces, or nanostructures. These elements are typically small in size and can be arranged in a planar array to form a large surface that can be placed on building surfaces, ceilings, and walls. The arrangement and tuning of the passive elements can be controlled through a centralized or distributed controller.

For example, RIS can be controlled using various methods, including analog control, digital control, and hybrid control.

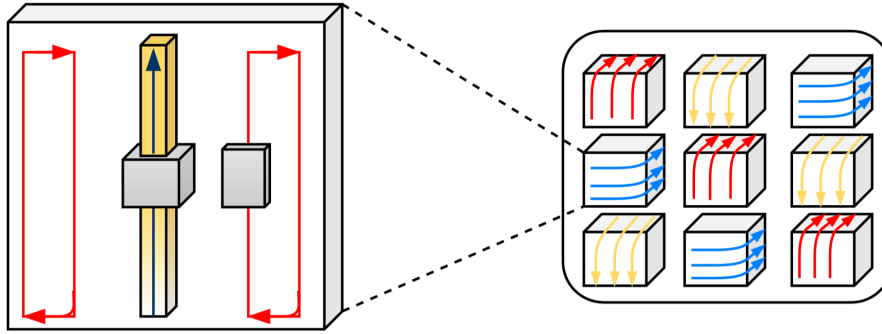


Figure 1.1: Structure and RIS operations relying on diodes.

In analog control, the phase shifters of the RIS are continuously adjustable and can be controlled by adjusting the voltage applied to them. The voltage is typically generated using digital-to-analog converters and analog circuits, allowing for smooth and continuous phase control. However, analog control has limited precision and can be susceptible to interference from other sources.

In digital control, the RIS elements are controlled by digital signals, which are generated by digital circuits and transmitted to the RIS using a digital communication interface. The digital control method provides high precision and is immune to interference, but it requires high-speed processing and transmission capabilities, which can increase the cost and complexity of the system.

Hybrid control combines both analog and digital control methods to take advantage of their respective strengths. In this method, the phase shifters are divided into groups, and each group is controlled by a separate digital-to-analog converter. The digital control is used to adjust the coarse phase shifts, while the analog control is used to fine-tune the phase shifts. Hybrid control provides a good balance between precision and complexity, making it a popular choice for RIS systems.

1.2 RIS in Wireless Communication

RIS technology has recently gained significant attention due to its potential to revolutionize wireless communication systems, especially in the beyond fifth-generation (5G) and sixth-generation (6G) [41, 36, 31, 3, 7]. RIS can significantly improve spectral efficiency, energy efficiency, and coverage by leveraging the additional degrees of freedom provided by the RIS to control the propagation environment [8, 20, 34]. Moreover, RIS can operate as an energy-efficient alternative to traditional wireless relays, which can be used to overcome excessive thermal noise and increase the overall system capacity. Additionally, RIS can be easily implemented in densely populated environments, such as urban areas, at a low cost [10, 30]. The small size and low weight of RIS reflectors also make them ideal for installation on building surfaces, ceilings, and walls.

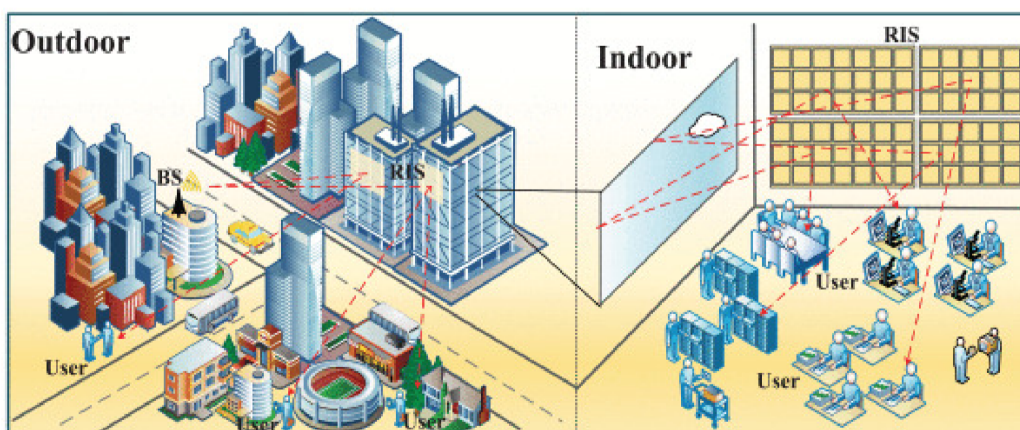


Figure 1.2: RIS applications.

One key advantage of RIS technology is the ability to adjust the phase shifts of the reflectors collaboratively, improving the received signal quality and reducing unwanted interference. However, analyzing the performance of RIS systems can be challenging, as the received signal-to-noise ratio (SNR) at the receiver is intrinsically affected by channel fading propagation and the phase-shift alignment

at the RIS [25, 23].

Despite these challenges, RIS technology has shown great promise in improving the performance of wireless communication systems. Several studies have demonstrated the benefits of using RIS, including increasing channel capacity and improving total transmit power consumption [32, 40, 46, 16, 43, 25]. Further research is needed to fully understand the potential of RIS technology and to develop new applications and deployment strategies that maximize its benefits.

1.3 An Example

Consider a simple RIS-aided single-input single-output system, as shown in Fig. 1. A transmitter (Tx) communicates with a receiver (Rx) via the help of a RIS with the K reflective element. Herein, assume that Tx cannot reach Rx since obstacles or far distance. The received signal at Rx is given by

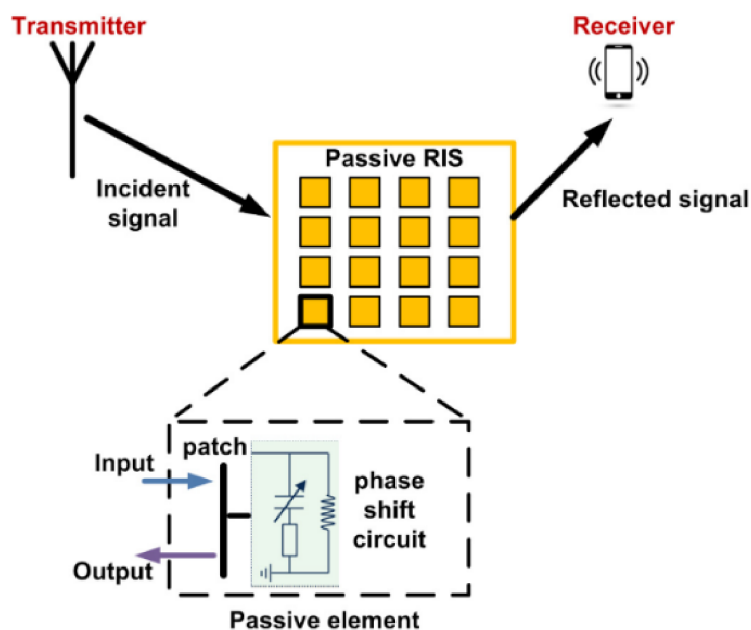


Figure 1.3: A single RIS-aided single-input single-output system.

$$y = \sqrt{P}\mathbf{h}\Phi\mathbf{g}x + n, \quad (1.1)$$

where P is transmit power, n is the additive white Gaussian noise with $\mathcal{CN} \sim (0, 1)$, $\Phi = [e^{j\phi_1}, \dots, e^{j\phi_K}]$ is the phase shift at RIS, and $\mathbf{h} = [h_1, \dots, h_K]$ and $\mathbf{g} = [g_1, \dots, g_K]$ are the channel matrices for the links of Tx \rightarrow RIS and RIS \rightarrow Rx, respectively. Each element of \mathbf{h} and \mathbf{g} are assumed to be subject to Rayleigh block-fading with zero-mean and the corresponding variances of Ω_h and Ω_g .

Therefore, the SNR for decoding x at Rx can be expressed as

$$\gamma = P|\mathbf{h}\Phi\mathbf{g}|^2 \quad (1.2)$$

According to (1.2), the cumulative distribution function (CDF) of γ can be evaluated in two aspects of phase design at RIS with the name of uncertain phase shift (UPS) and optimal phase shift (OPS).

- OPS scenario

Aiming to enhance the channel quality at Rx, since the phase shift at the RIS can be optimized as $\Phi = -\arg(\mathbf{h}) - \arg(\mathbf{g})$ [27, 28, 37]. Then, a closed-form expression for the CDF of Rx with OPS can be expressed as

$$F_O = \frac{\gamma(k_O, \sqrt{x}/w_O)}{\Gamma(k_O)}, \quad (1.3)$$

where $\Gamma(a)$ is gamma function [12, Eq. (8.31)], $\gamma(a, b)$ is the lower incomplete gamma function [12, Eq. (8.35)], $k_O = \frac{\pi^2}{16-\pi^2}$ and $w_O = \frac{K(16-\pi^2)\sqrt{\Omega_h\Omega_g}}{4\pi}$ are shape and scale parameters, respectively.

- UPS scenario For the UPS configuration, Φ can be considered as $\Phi \sim [0, 2\pi]$. Therefore, a closed-form expression for the CDF of Rx with UPS can be

expressed as

$$F_U = \frac{\gamma(k_U, x/w_U)}{\Gamma(k_U)}, \quad (1.4)$$

where $k_U = 1$ and $w_U = K\Omega_h\Omega_g$ are shape and scale parameters, respectively.

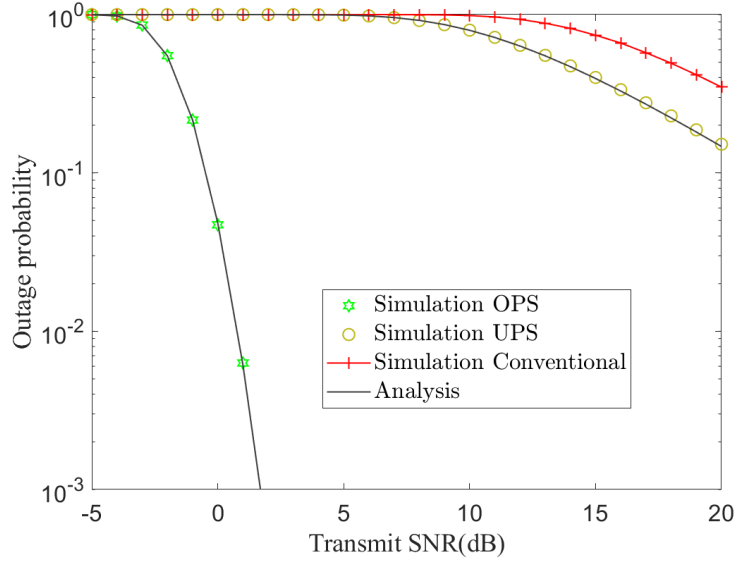


Figure 1.4: A comparison of RIS and conventional systems.

Following (1.3) and (1.4), Fig. 1.4 plots the outage probability (OP) comparison between RIS systems and conventional systems with $K = 40$. As can be observed, the OPS method outperforms both the UPS and the conventional methods, while the UPS method demonstrates slightly better performance than the conventional method. Notably, at an outage probability of 10^{-1} , the gap between the OPS curve and the UPS curve, the OPS curve and the conventional curve, and the UPS curve and the conventional curve are 20 dB, more than 20 dB, and 5 dB, respectively. This indicates that the use of RIS can significantly enhance the performance of the system, especially in the case of OPS.

1.4 Organization

The rest of this thesis is organized as follows. Section II explores the system model and OP analysis. Section III provides the numerical results and discussions. Finally, Section IV summarizes the conclusions of this thesis.

Chapter 2

Performance Analysis of Multiple RIS-aided Wireless Communication Networks

Recent studies have explored various aspects of RIS-enabled wireless networks, such as network architecture from a single-input single-output (SISO) [6, 14, 38, 4] and multiple-input single-output (MISO) systems [1, 19, 26, 17, 13, 2, 29], to multiple-input multiple-output (MIMO) system [15, 5]; or network application: green communication [18], full-duplex communication [33], physical security [11, 35], and cognitive radio [42, 24]. In the aspect of network architectures, the authors in [6] carried out a performance comparison between RIS and conventional relaying systems. To maximize the ergodic spectral efficiency, the authors in [14] proposed the upper bound OPS by exploiting statistical channel state information (CSI). In [38], the authors examined the effect of successive interference cancellation imperfections under two scenarios of optimal and UPS alignment. In [4], the authors addressed the question of how many surfaces for RIS are sufficient to beat the decode-and-forward relaying. For simple MISO systems, the authors in [1]

and [19] investigated the design of beamforming vector and practical phase-shift model along with beamforming, respectively. In contrast, the authors in [26] separately focused on multi-group multicast and multiple-user communications. To reduce the complex analysis, the asymptotic expressions for OP and the signal-to-interference-plus-noise ratio were derived in [17] and in [13, 2], respectively. Looking at the potential of data transmission with a massive number of sensing and radiating elements, a new concept of a large intelligent surface associated with massive MIMO (mMIMO) technology has been introduced in [15]. Similarly, a new thoughtful consideration for the next future direction of RIS-aided mMIMO was put forward in [5]. Regarding network application, the authors in [18] proposed two novel MIMO schemes, namely Vertical Bell Labs layered space-time and Alamouti, for simple RIS-based transceiver architecture to enhance the SE. For a full-duplex RIS-based system, the authors of [33] have formulated the sum rate optimization problem by optimizing the energy splitting and mode switching protocols. Because of such a non-convex optimization problem, successive convex approximation technique has been employed to obtain sub-optimal solutions. Considering the existence of multi-antenna eavesdroppers, the authors in [11] jointly designed the transmit covariance matrix at the transmitter and the phase-shift matrix at the RIS to maximize the secrecy rate of wiretap channels. In [35], the authors quantified the impact of phase-shift error on secrecy outage and capacity under different scaling laws of the legitimate and eavesdroppers SNR and the number of RIS reflectors. In [24], the authors provided the analytical results with two scenarios of RIS configurations access point RIS and RIS relay to indicate how the user of RIS configurations by primary users can improve the network performance. Finally, the authors in [42] optimized the transmit precoding at the secondary transceiver and the phase-shift of RIS to minimize the budget transmit power constrained by the quality of secondary user services, and the interference

links.

Although the studies in [6, 14, 38, 4, 1, 19, 26, 17, 13, 2, 15, 5] have provided significant contributions to the field of RISs with SISO, MISO, and MIMO systems, these works still have some limitations that need further in-depth investigation. Firstly, the RIS is typically constructed with multiple arrays distributed close together in practice and has been only explored for SISO systems in [6, 14, 38, 4]. So that, the application of multi-RIS still has many rooms that need to be fulfilled. Secondly, the previous works of [1, 19, 26, 17, 13, 2] mainly focused on optimizing the beamforming vector design with the OPS at RISs under the conditions of perfect [1, 19, 26, 17] or imperfect CSI [2] but lacked theoretical analysis for multiple antenna transceiver systems (i.e., MISO or MIMO) due to complex mathematical problems. Therefore, it becomes essential to provide analysis guidance to gain some useful technical insights. Thirdly, only the authors of [33] considered the optimization of both uplink and downlink with the full-duplex system, while all the existing works of [17, 13, 2, 21, 44] stopped at the investigation of downlink [17, 13, 2] or uplink systems [21, 44], and there has been no comprehensive work considering the analysis of both downlink and uplink systems. Finally, it is well-known that RIS is an emerging technology to enhance the system's performance without direct links between source and user. Therefore, various existing researchers have designed and optimized their network's performance with this worst-case scenario. However, it is not totally valid in practice since the user is mobile, and thus wireless communication can exist on both direct and reflective paths. In this case, designing a beamforming vector raises the crucial question "Should the direct path or the reflective path be focused on?" So far, this remains an open question.

Motivated by the aforementioned above as well as to fulfill these existing gaps in the literature, this chapter investigates the performance analysis of down-

link/uplink RIS-aided wireless systems, where the base station (B) communicates with the user via both direct link and one optimal RIS selected among a set of distributed RISs. The main contributions of this paper can be summarized as follows:

- Firstly, this thesis investigates the performance of downlink/uplink RIS-aided wireless systems over Rayleigh fading channels under two scenarios of UPS and OPS alignment at RIS. In uplink systems, this work assesses two schemes of maximal ratio combining (MRC) and selection combining (SC) at the B. In downlink systems, two schemes of beamforming vector design along with maximal ratio transmission (MRT) are considered at the B, namely direct-path beamforming design (DBD) and reflective-path beamforming design (RBD).
- Secondly, the OP with UPS and OPS for each transmission mode (i.e., uplink and downlink) are evaluated. Specifically, for uplink systems, we present the CDF corresponding to the MRC and SC schemes. For downlink systems, we approximate a probability density function (PDF) for the channel random variable using direct-path beamforming design (DBD) and reflective-path beamforming design (RBD) schemes. Based on the obtained PDFs and CDFs, we then derive the closed-form expressions for the OP of each system consideration.
- Finally, extensive simulations were conducted to validate the accuracy of the theoretical analysis results and to provide technical insights. Specifically, the simulations focused on examining the impact of various factors, including the antenna configuration at B, the number of distributed RISs, and the number of RIS units. Additionally, all results quantified the performance difference between using UPS and OPS for both uplink and downlink models. Based

on the numerical results, several observations were made: (1) For uplink transmission, the best performance was achieved when employing MRC at the B and OPS at the RIS. When using OPS, SC can provide exceptional performance for small antenna configurations compared to MRC-integrated UPS. (2) For downlink transmission, RBD outperformed DBD. Using OPS with RBD also achieved better performance than using UPS.

2.1 Uplink System model

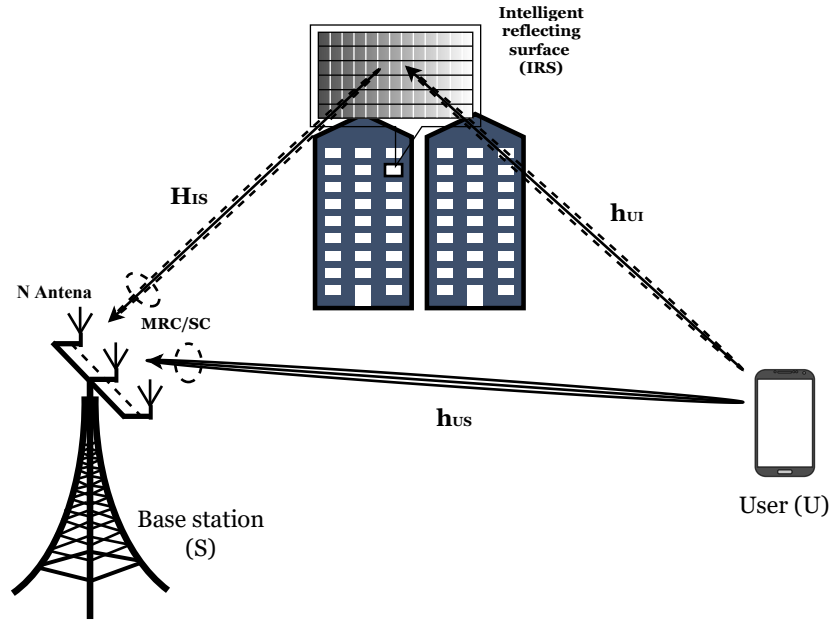


Figure 2.1: Uplink model

As presented in Fig.1, we consider an uplink RIS-based wireless system, which includes one B with N antennas to serve one single-antenna user (U) through the assistance of one RIS selected among a set of M RIS, each of them having K passive elements. Considering far-field regions, since the distance between the direct and non-direct links is non-identical, the signals passing over direct and non-direct

links are not simultaneously received at the receiver [4]. Throughout this paper, we assume that perfect knowledge of CSI is available at the terminals by using the least mean-square-error method at the B and error-free feedback channel at the U [17]. All elements in the RIS are uniformly distributed with half a wavelength, and there is no signal correlation or association from one element to another [37].

2.1.1 Channel Model Description

Let us denote $\mathbf{H}_{\text{RB}} = [h_{\text{RB}}^{1,1}, \dots, h_{\text{RB}}^{1,K}; \dots; h_{\text{RB}}^{N,1}, \dots, h_{\text{RB}}^{N,K}]$, $\mathbf{h}_{\text{UR}} = [h_{\text{UR}}^1, \dots, h_{\text{UR}}^K]$, and $\mathbf{h}_{\text{UB}} = [h_{\text{UB}}^1, \dots, h_{\text{UB}}^N]$ are the channel matrices for the links of RIS \rightarrow B, U \rightarrow RIS, and U \rightarrow B, respectively. Each element of \mathbf{H}_{RB} , \mathbf{h}_{UR} , \mathbf{h}_{UB} and are assumed to be subject to Rayleigh block-fading with zero-mean and the corresponding variances of Ω_{RB} , Ω_{UR} , and Ω_{UB} . Also, $\Phi = \text{diag}(e^{j\phi_1}, \dots, e^{j\phi_K})$ is the diagonal phase-shift matrix at RIS for $\phi_k \in (0, 2\pi]$ and $k \in \{1, \dots, K\}$.

In the uplink transmission, U sends signal $x = \sqrt{P}x_U$ to B through both direct and non-direct links after employing the RIS selection strategy with SC and MRC, which can be mathematically explained as

$$a = \arg \max_{n=1, \dots, N} \|h_{\text{UB}}^n\|^2, \quad (2.1)$$

$$(b, c) = \arg \max_{\substack{n=1, \dots, N \\ m=1, \dots, M}} \left\| \sum_{k=1}^K \left(h_{\text{UR}}^{n,k} e^{j\phi_k} H_{\text{RB}}^{n,k} \right)_m \right\|^2, \quad (2.2)$$

and

$$d = \arg \max_{m=1, \dots, M} \|(\mathbf{h}_{\text{UR}} \Phi \mathbf{H}_{\text{RB}})_m\|^2. \quad (2.3)$$

Following that, the received signal at B with SC and MRC can be expressed, respectively, as

$$y_{\text{SC}} = h_{\text{UB}}^a \sqrt{P}x + \sum_{k=1}^K \left(h_{\text{UR}}^{b,k} e^{j\phi_k} H_{\text{RB}}^{b,k} \right)_c \sqrt{P}x + n \quad (2.4)$$

and

$$\begin{aligned} y_{\text{MRC}} &= \mathbf{h}_{\text{UB}} \sqrt{P}x + (\mathbf{h}_{\text{UR}} \Phi \mathbf{H}_{\text{RB}})_d \sqrt{P}x + n \\ &= \sum_{n=1}^N h_{\text{UB}}^n \sqrt{P}x + \sum_{n=1}^N \left(\sum_{k=1}^K h_{\text{UR}}^{n,k} e^{j\phi_k} H_{\text{RB}}^{n,k} \right)_d \sqrt{P}x + n, \end{aligned} \quad (2.5)$$

where P is the transmit power of U, x is signal symbol, $\text{E}[|x|^2] = 1$, and n is the additive white Gaussian noise with $\mathcal{CN}(0, \sigma^2 \mathbf{I})$ and a $1 \times N$ identity vector \mathbf{I} .

Let $\gamma_{\text{SC1}} = |h_{\text{UB}}^a|$, $\gamma_{\text{SC2}} = \left| \sum_{k=1}^K \left(h_{\text{UR}}^{b,k} e^{j\phi_k} H_{\text{RB}}^{b,k} \right)_c \right|$, $\gamma_{\text{MRC1}} = \|\mathbf{h}_{\text{UB}}\|$, and $\gamma_{\text{MRC2}} = \|(\mathbf{h}_{\text{UR}} \Phi \mathbf{H}_{\text{RB}})_d\|$. From (4), the SNR for decoding x at the B by using the SC scheme can be expressed as

$$\begin{aligned} \gamma_{\text{SC}} &= \frac{P}{\sigma^2} \left[|h_{\text{UB}}^a|^2 + \left| \left(\sum_{k=1}^K h_{\text{UR}}^{b,k} e^{j\phi_k} h_{\text{RB}}^{b,k} \right)_c \right|^2 \right] \\ &= \rho (\gamma_{\text{SC1}}^2 + \gamma_{\text{SC2}}^2), \end{aligned} \quad (2.6)$$

where $\rho = P/\sigma^2$, the a -th and b -th antennas, the c -th RIS are selected, respectively. Meanwhile, the received SNR by using the MRC scheme at B can be expressed as

$$\begin{aligned} \gamma_{\text{MRC}} &= \frac{P}{\sigma^2} [\|\mathbf{h}_{\text{UB}}\|^2 + \|(\mathbf{h}_{\text{UR}} \Phi \mathbf{h}_{\text{RB}})_d\|^2] \\ &= \frac{P}{\sigma^2} (\gamma_{\text{MRC1}}^2 + \gamma_{\text{MRC2}}^2), \end{aligned} \quad (2.7)$$

$$\varepsilon(\tau_1, \tau_2, \tau_3, \tau_4) = \begin{cases} \left(\frac{1}{\Gamma(\tau_4)}\right)^{\tau_2}, & \tau_1 = 0, \\ \frac{\Gamma(\tau_4)}{\tau_1} \sum_{k=1}^{\tau_1} (k\tau_2 - \tau_1 + k) \frac{\varepsilon(\tau_1-k, \tau_2, \tau_3, \tau_4)}{(\tau_3^k \Gamma(\tau_4+k+1))}, & \text{Otherwise.} \end{cases} \quad (2.8)$$

where d represents the d -th RIS.

2.1.2 Outage Probability Analysis

This section focuses on deriving the closed-form OP expressions under uplink/downlink transmission. In order to simplify the formulation as well as the presentation, we first provide self-defined recursive functions as in (2.8), shown at the top of the next page.

Next, the outage event is defined as the probability that the SNR received γ_i with $i \in \{\text{SC}, \text{MRC}, \text{DBD}, \text{RBD}\}$ at the receiver is less than a given threshold $\gamma_{th} = 2^{\mathcal{R}} - 1$, where \mathcal{R} refers to the target data rate.

Outage performance of SC:

From (2.6) and outage event definitions, the OP to decode x when employing SC at the B can be expressed as

$$OP_{\text{SC}} = \Pr(\gamma_{\text{SC}} < \gamma_{th}). \quad (2.9)$$

Lemma 1: The closed-form expression for the OP with SC configuration at the B and UPS alignment at the RIS can be derived as

$$OP_{\text{SC,U}} = \sum_{n=0}^N \sum_{m=0}^{MN-1} \frac{(-1)^{n+m} C_n^N C_m^{MN-1} MN \Omega_{\text{UB}}}{(m+1) \Omega_{\text{UB}} - n \Omega_{\text{URB}}} \times \left[\exp\left(-\frac{n \gamma_{th}}{\rho \Omega_{\text{UB}}}\right) - \exp\left(\gamma_{th} \frac{n \Omega_{\text{URB}} - (m+1) \Omega_{\text{UB}}}{\rho \Omega_{\text{UB}} \Omega_{\text{URB}}}\right) \right], \quad (2.10)$$

where $\Omega_{\text{URB}} = K\Omega_{\text{UR}}\Omega_{\text{RB}}$.

Proof: Since the best antenna is chosen based on the best channel capacity, the CDF of direct link γ_{SC1}^2 is provided as

$$F_{\gamma_{\text{SC1}}^2}(x) = \left[1 - \exp\left(-\frac{x}{\Omega_{\text{UB}}}\right)\right]^N. \quad (2.11)$$

For UPS, the non-direct link can be approximated to $\gamma_{\text{SC2,U}} = \left|\sum_{k=1}^K \left(h_{\text{UR}}^{b,k} H_{\text{RB}}^{b,k}\right)_c\right|$ with $e^{j\phi_k} = 0$. Thus, the PDF of $\gamma_{\text{SC2,U}}^2$ is provided as

$$f_{\gamma_{\text{SC2,U}}^2}(x) = \frac{MN}{\Omega_{\text{URB}}} \exp\left(-\frac{x}{\Omega_{\text{URB}}}\right) \left[1 - \exp\left(-\frac{x}{\Omega_{\text{URB}}}\right)\right]^{MN-1}. \quad (2.12)$$

From (2.6), the OP of $\gamma_{\text{SC,U}}$ for RPS can be written as

$$OP_{\text{SC,U}} = \int_0^{\gamma_{\text{th}}/\rho} F_{\gamma_{\text{SC1}}^2}\left(\frac{\gamma_{\text{th}}}{\rho} - x\right) f_{\gamma_{\text{SC2,U}}^2}(x) dx \quad (2.13)$$

$$= \int_0^{\gamma_{\text{th}}/\rho} \left[1 - \exp\left(-\frac{\gamma_{\text{th}}}{\rho} + \frac{x}{\Omega_{\text{UB}}}\right)\right]^N \frac{MN}{\Omega_{\text{URB}}} \times \exp\left(-\frac{x}{\Omega_{\text{URB}}}\right) \left[1 - \exp\left(-\frac{x}{\Omega_{\text{URB}}}\right)\right]^{MN-1} dx \quad (2.14)$$

$$= \int_0^{\gamma_{\text{th}}/\rho} \sum_{n=0}^N \sum_{m=0}^{NM-1} C_n^N C_m^{NM-1} \exp\left(-\frac{n\gamma_{\text{th}}}{\rho\Omega_{\text{UB}}}\right) \times (-1)^{n+m} \exp\left(x \frac{n\Omega_{\text{URB}} - (m+1)\Omega_{\text{UB}}}{\Omega_{\text{UB}}\Omega_{\text{URB}}}\right) dx, \quad (2.15)$$

where $C_r^R = R!/[(R-r)!r!]$. The proof is completed.

Corollary 1: To provide some insights into the considered system, we carry out the asymptotic analysis for the OP when transmit SNR goes to infinity, i.e., $\rho \rightarrow \infty$ by using the Maclaurin expansion for $\exp(-x/\rho)$ as

$$\exp\left(-\frac{x}{\rho}\right) \sim \sum_{r=0}^R \frac{(-x/\rho)^r}{r!}, \quad (2.16)$$

where R is the expansion order. Therewith, the asymptotic of $OP_{\text{SC,U}}$ can be expressed as

$$\begin{aligned} OP_{\text{SC,U}}^{\text{Asym}} &= \sum_{n=0}^N \sum_{m=0}^{MN-1} \frac{(-1)^{m+n} C_n^N C_m^{MN-1} MN \Omega_{\text{UB}}}{(m+1)\Omega_{\text{UB}} - n\Omega_{\text{URB}}} \\ &\times \sum_{r=0}^R \frac{[-n\gamma_{th}/(\rho\Omega_{\text{UB}})]^r - \left[\frac{\gamma_{th}[n\Omega_{\text{URB}} - (m+1)\Omega_{\text{UB}}]}{\rho\Omega_{\text{UB}}\Omega_{\text{URB}}}\right]^r}{r!}. \end{aligned} \quad (2.17)$$

Lemma 2: The closed-form expression for the OP with SC configuration at the B and OPS alignment at the RIS can be derived as

$$OP_{\text{SC,O}} = \left(\frac{\Upsilon\left(k_{\text{SC}}, \frac{\sqrt{\gamma_{th}/\rho}}{w_{\text{SC}}}\right)}{\Gamma(k_{\text{SC}})} \right)^{MN} + \Xi_{\text{SC}}, \quad (2.18)$$

where $\Upsilon(n, a) = \int_0^a t^{n-1} \exp(-t) dt$ refers to the lower incomplete Gamma function [12, Eq. (8.350.1)]. $k_{\text{SC}} = K\pi^2/[16 - \pi^2]$, $w_{\text{SC}} = (16 - \pi^2)\sqrt{\Omega_{\text{UR}}\Omega_{\text{RB}}}/[4\pi]$ are the shape and scale parameters of the Gamma distribution, and Ξ_{SC} is determined as

$$\Xi_{\text{SC}} = \frac{\gamma_{th}\pi}{\rho 2L} \sum_{l=0}^L \sum_{n=1}^N \sqrt{1 - \vartheta} \sum_{n=1}^N C_n^N (-1)^n \exp\left(-\frac{n\gamma_{th}}{\rho\Omega_{\text{UB}}} + \frac{n\eta}{\Omega_{\text{UB}}}\right) f_{\gamma_{\text{SC2,O}}^2}(\eta) dx, \quad (2.19)$$

where L is the complexity accuracy trade-off parameter, $\vartheta = \cos(\pi[2l-1]/2L)$ and $\eta = \gamma_{th}(\vartheta + 1)/(2\rho)$.

Proof: For the OPS with RIS is selected, the γ_{SC2} can be approximated to $\gamma_{\text{SC2,O}} = \left| \sum_{k=1}^K \left[\left| h_{\text{UR}}^{b,k} \right| \left| H_{\text{RB}}^{b,k} \right| \right]_c \right|$. According to [38], we can easily determine the shape

parameter k_{SC} and scale parameter w_{SC} of the Gamma distribution by using the moment-matching method. Thus, PDF and CDF of $\gamma_{\text{SC}2,\text{O}}^2$ can be provided as

$$f_{\gamma_{\text{SC}2,\text{O}}^2}(x) = \frac{MN(\sqrt{x})^{k_{\text{SC}}-2}}{2\Gamma(k_{\text{SC}})w_{\text{SC}}^{k_{\text{SC}}}} \exp\left(-\frac{\sqrt{x}}{w_{\text{SC}}}\right) \left[\frac{\Upsilon\left(k_{\text{SC}}, \frac{\sqrt{x}}{w_{\text{SC}}}\right)}{\Gamma(k_{\text{SC}})}\right]^{MN-1} \quad (2.20)$$

and

$$F_{\gamma_{\text{SC}2,\text{O}}^2}(x) = \left[\frac{\Upsilon\left(k_{\text{SC}}, \frac{\sqrt{x}}{w_{\text{SC}}}\right)}{\Gamma(k_{\text{SC}})}\right]^{MN}. \quad (2.21)$$

Combining (2.11) with (2.20) and (2.21) the OP of $\gamma_{\text{SC},\text{O}}$ can be written as

$$OP_{\text{SC},\text{O}} = \int_0^{\gamma_{\text{th}}/\rho} F_{\gamma_{\text{SC}1}^2}\left(\frac{\gamma_{\text{th}}}{\rho} - x\right) f_{\gamma_{\text{SC}2,\text{O}}^2}(x) dx \quad (2.22)$$

$$= \int_0^{\gamma_{\text{th}}/\rho} \left[1 - \exp\left(-\frac{\gamma_{\text{th}} - x}{\Omega_{\text{UB}}}\right)\right]^N f_{\gamma_{\text{SC}2,\text{O}}^2}(x) dx \quad (2.23)$$

$$= \frac{\Upsilon\left(k_{\text{SC}}, \frac{\sqrt{\gamma_{\text{th}}/\rho}}{w_{\text{SC}}}\right)^{MN}}{\Gamma(k_{\text{SC}})^{MN}} + \int_0^{\gamma_{\text{th}}/\rho} \sum_{n=1}^N C_n^N (-1)^n \exp\left(-\frac{\gamma_{\text{th}} - x}{\Omega_{\text{UB}}}\right)^n f_{\gamma_{\text{SC}2,\text{O}}^2}(x) dx. \quad (2.24)$$

At high SNR regime, since $\rho \rightarrow \infty$ (i.e., $\gamma_{\text{th}}/\rho \rightarrow 0$), the integral of the right-hand side becomes zero. Besides, $f_{\gamma_{\text{SC}2,\text{O}}^2}(x)$ contains \sqrt{x} ; thus, it is quite challenging to directly solve (2.24). To overcome this hurdle, we rely on the Gaussian-Chebyshev quadrature method [39, Eq. (45)]. The proof is completed.

Corollary 2: Applying [12, Eq. (8.354.1)] for (2.18), when $\rho \rightarrow \infty$, the asymptotic of $OP_{\text{SC},\text{O}}$ can be expressed as

$$OP_{\text{SC},\text{O}}^{\text{Asym}} = \left[\frac{[\gamma_{th}/(\rho w_{\text{SC}}^2)]^{k_{\text{SC}}/2}}{k_{\text{SC}}\Gamma(k_{\text{SC}})} \right]^{MN}. \quad (2.25)$$

The $OP_{\text{SC},\text{O}}^{\text{Asym}}$ in (21) shows that the diversity order of OPS design is $MNk_{\text{SC}}/2$.

Outage performance of MRC:

From (2.7) and outage event definitions, the OP to decode x when employing MRC at the B can be expressed as

$$OP_{\text{MRC}} = \Pr(\gamma_{\text{MRC}} < \gamma_{th}). \quad (2.26)$$

Lemma 3: The closed-form expression for the OP with MRC configuration at the B and UPS alignment at the RIS can be derived as

$$OP_{\text{MRC},\text{U}} = \frac{\sum_{t=0}^{\infty} \sum_{n=0}^{N-1} \varepsilon(\tau_1, \tau_2, \tau_3, \tau_4) (-1)^n C_n^{N-1} \mu_1^{-v_1}}{\Omega_{\text{UB}}^N \Omega_{\text{URB}}^{MN} \Gamma(N)} \times \exp\left(-\frac{\gamma_{th}}{\rho \Omega_{\text{UB}}}\right) \left(\frac{\gamma_{th}}{\rho}\right)^{N-n-1} \Upsilon\left(v_1, \frac{\mu_1 \gamma_{th}}{\rho}\right) \quad (2.27)$$

where $\mu_1 = [M\Omega_{\text{UB}} - \Omega_{\text{URB}}]/[\Omega_{\text{UB}}\Omega_{\text{URB}}]$, $v_1 = MN + t + n + 1$, and the entries of the recursive function $\varepsilon(\tau_1, \tau_2, \tau_3, \tau_4)$ are set as $\tau_1 = t$, $\tau_2 = M$, $\tau_3 = \Omega_{\text{URB}}$, and $\tau_4 = N$.

Proof: For MRC, the PDF and CDF of γ_{MRC1}^2 can be expressed as

$$f_{\gamma_{\text{MRC1}}^2}(x) = \frac{x^{N-1}}{\Gamma(N) \Omega_{\text{UB}}^N} \exp\left(-\frac{x}{\Omega_{\text{UB}}}\right) \quad (2.28)$$

and

$$F_{\gamma_{\text{MRC1}}^2}(x) = \frac{\Upsilon\left(N, \frac{x}{\Omega_{\text{UB}}}\right)}{\Gamma(N)}. \quad (2.29)$$

For UPS combined with MRC scheme, the non-direct link can be approximated to $\gamma_{\text{MRC2,U}} = \|\mathbf{h}_{\text{UR}}\mathbf{H}_{\text{RB}}\|_d$. The CDF and PDF of $\gamma_{\text{MRC2,U}}^2$ can be expressed as

$$F_{\gamma_{\text{MRC2,U}}^2}(x) = \left[\Upsilon\left(N, \frac{x}{\Omega_{\text{URB}}}\right) / \Gamma(N) \right]^M \quad (2.30)$$

and

$$f_{\gamma_{\text{MRC2,U}}^2}(x) = \frac{M x^{N-1}}{\Omega_{\text{URB}}^N \Gamma(N)} \exp\left(-\frac{x}{\Omega_{\text{URB}}}\right) \left[\frac{\Upsilon\left(N, \frac{x}{\Omega_{\text{URB}}}\right)}{\Gamma(N)} \right]^{M-1}. \quad (2.31)$$

From (2.7), the OP of $\gamma_{\text{MRC,U}}$ can be written as

$$OP_{\text{MRC,U}} = \int_0^{\gamma_{th}/\rho} F_{\gamma_{\text{MRC2,U}}^2}\left(\frac{\gamma_{th}}{\rho} - y\right) f_{\gamma_{\text{MRC1}}^2}(y) dy \quad (2.32)$$

$$= \int_0^{\gamma_{th}/\rho} \left[\frac{\Upsilon\left(N, \frac{\gamma_{th}/\rho - y}{\Omega_{\text{URB}}}\right)}{\Gamma(N)} \right]^M \frac{y^{N-1}}{\Gamma(N) \Omega_{\text{UB}}^N} \exp\left(-\frac{y}{\Omega_{\text{UB}}}\right) dy. \quad (2.33)$$

Let $\gamma_{th}/\rho - y = x$, the integral of (2.33) can be expressed as

$$OP_{\text{MRC,U}} = \int_0^{\gamma_{th}/\rho} \left[\frac{\Upsilon\left(N, \frac{x}{\Omega_{\text{URB}}}\right)}{\Gamma(N)} \right]^M \frac{\left(\frac{\gamma_{th}}{\rho} - x\right)^{N-1}}{\Gamma(N) \Omega_{\text{UB}}^N} \exp\left(-\frac{\gamma_{th}}{\rho \Omega_{\text{UB}}} + \frac{x}{\Omega_{\text{UB}}}\right) dx \quad (2.34)$$

$$\begin{aligned} &= \int_0^{\gamma_{th}/\rho} \left(\frac{x}{\Omega_{\text{URB}}}\right)^{NM} \left[\sum_{t=0}^{\infty} \frac{x^t}{\Omega_{\text{URB}}^t \Gamma(N+t+1)} \right]^M \\ &\times \frac{\sum_{n=0}^{N-1} \left(\frac{\gamma_{th}}{\rho}\right)^{N-n-1} (-1)^n C_n^{N-1} x^n}{\Gamma(N) \Omega_{\text{UB}}^N} \exp\left(-\frac{\gamma_{th}}{\rho \Omega_{\text{UB}}} - x \frac{M \Omega_{\text{UB}} - \Omega_{\text{URB}}}{\Omega_{\text{UB}} \Omega_{\text{URB}}}\right) dx \end{aligned} \quad (2.35)$$

$$\begin{aligned}
&= \int_0^{\gamma_{th}/\rho} \sum_{n=0}^{N-1} \sum_{t=0}^{\infty} \frac{\varepsilon(\tau_1, \tau_2, \tau_3, \tau_4) C_n^{N-1} (-1)^n}{\Gamma(N) \Omega_{\text{UB}}^N \Omega_{\text{URB}}^{NM}} \\
&\times \exp\left(-\frac{\gamma_{th}}{\rho \Omega_{\text{UB}}}\right) \left(\frac{\gamma_{th}}{\rho}\right)^{N-n-1} x^{NM+t+n} \exp\left(-x \frac{M\Omega_{\text{UB}} - \Omega_{\text{URB}}}{\Omega_{\text{UB}} \Omega_{\text{URB}}}\right) dx. \quad (2.36)
\end{aligned}$$

By using [12, Eq. (3.381.1)], the closed-form expression for OP of $\gamma_{\text{MRC,R}}$ can be achieved as in (2.27). The proof is completed.

Corollary 3: Similar to (2.21) and (2.25), when $\rho \rightarrow \infty$, the asymptotic of $OP_{\text{MRC,U}}$ can be expressed as

$$\begin{aligned}
OP_{\text{MRC,U}}^{\text{Asym}} &= \sum_{t=0}^{\infty} \sum_{n=0}^{N-1} \frac{\varepsilon(\tau_1, \tau_2, \tau_3, \tau_4) (-1)^n C_n^{N-1} \mu_1^{-v_1}}{\Omega_{\text{UB}}^N \Omega_{\text{URB}}^{MN} \Gamma(N)} \\
&\times \frac{(\gamma_{th} \mu_1 / \rho)^{v_1}}{v_1 \Gamma(v_1)} \sum_{r=0}^R \frac{[-\gamma_{th} / (\rho \Omega_{\text{UB}})]^r}{r!} \left(\frac{\gamma_{th}}{\rho}\right)^{N-n-1}. \quad (2.37)
\end{aligned}$$

Remark 1: We can see that $OP_{\text{MRC,U}}$ consists of infinite series. For more detailed insights, we consider the $OP_{\text{MRC,U}}^{\text{Ana}}/OP_{\text{MRC,U}}^{\text{Sim}}$ ratio to show the convergence of (2.27).

Lemma 4: The closed-form expression for the OP with MRC configuration at the B and OPS alignment at the RIS can be derived as

$$OP_{\text{MRC,O}} = \left[\frac{\Upsilon\left(k_{\text{MRC}}, \frac{\sqrt{\gamma_{th}/\rho}}{w_{\text{MRC}}}\right)}{\Gamma(k_{\text{MRC}})} \right]^M - \Xi_{\text{MRC}}, \quad (2.38)$$

where $k_{\text{MRC}} = NK\pi^2/[16 - \pi^2]$ and $w_{\text{MRC}} = (16 - \pi^2) \sqrt{\Omega_{\text{UR}} \Omega_{\text{RB}}} / [4\pi\sqrt{N}]$ are the shape and scale parameters, and Ξ_{MRC} is determined as

$$\Xi_{\text{MRC}} = \frac{\gamma_{th}\pi}{\rho 2L} \sum_{l=1}^L \sqrt{1-\vartheta} (-1)^n \frac{\Gamma\left(N, \frac{\gamma_{th}/\rho-\eta}{\Omega_{\text{UB}}}\right)}{\Gamma(N)} f_{\gamma_{\text{MRC2,O}}^2}(\eta). \quad (2.39)$$

Proof: The γ_{MRC2} can be approximated to $\gamma_{\text{MRC2,O}} = \|\mathbf{h}_{\text{UR}}\|\|\mathbf{H}_{\text{RB}}\|_d$, the CDF and PDF of $\gamma_{\text{MRC2,O}}^2$ can be expressed as

$$F_{\gamma_{\text{MRC2,O}}^2}(x) = \left[\frac{\Upsilon\left(k_{\text{MRC}}, \frac{\sqrt{x}}{w_{\text{MRC}}}\right)}{\Gamma(k_{\text{MRC}})} \right]^M \quad (2.40)$$

and

$$f_{\gamma_{\text{MRC2,O}}^2}(x) = \frac{M(\sqrt{x})^{k_{\text{MRC}}-2}}{2\Gamma(k_{\text{MRC}})(w_{\text{MRC}})^{k_{\text{MRC}}}} \exp\left(-\frac{\sqrt{x}}{w_{\text{MRC}}}\right) \left[\frac{\Upsilon\left(k_{\text{MRC}}, \frac{\sqrt{x}}{w_{\text{MRC}}}\right)}{\Gamma(k_{\text{MRC}})} \right]^{M-1}. \quad (2.41)$$

By combining (2.29) with (2.40), the OP of $\gamma_{\text{MRC,O}}$ is expressed as

$$OP_{\text{MRC,O}} = \int_0^{\gamma_{th}/\rho} F_{\gamma_{\text{MRC1}}^2}\left(\frac{\gamma_{th}}{\rho} - x\right) f_{\gamma_{\text{MRC2,O}}^2}(x) dx \quad (2.42)$$

$$= \int_0^{\gamma_{th}/\rho} \left[1 - \frac{\Gamma\left(N, \frac{\gamma_{th}/\rho-x}{\Omega_{\text{UB}}}\right)}{\Gamma(N)} \right] f_{\gamma_{\text{MRC2,O}}^2}(x) dx \quad (2.43)$$

$$= \left[\frac{\Upsilon\left(k_{\text{MRC}}, \frac{\sqrt{x}}{w_{\text{MRC}}}\right)}{\Gamma(k_{\text{MRC}})} \right]^M - \int_0^{\gamma_{th}/\rho} \frac{\Gamma\left(N, \frac{\gamma_{th}/\rho-x}{\Omega_{\text{UB}}}\right)}{\Gamma(N)} f_{\gamma_{\text{MRC2,O}}^2}(x) dx. \quad (2.44)$$

Similar to Lemma 2, to overcome this hurdle, we rely on the Gaussian-Chebyshev quadrature method. The proof is completed.

Corollary 4: Applying [12, Eq. (8.354.1)] for (2.38), when $\rho \rightarrow \infty$, the asymp-

otic of $OP_{\text{MRC},0}$ can be expressed as

$$OP_{\text{MRC},0}^{\text{Asym}} = \left[\frac{[\gamma_{th}/(\rho w_{\text{MRC}}^2)]^{k_{\text{MRC}}/2}}{k_{\text{MRC}}\Gamma(k_{\text{MRC}})} \right]^M. \quad (2.45)$$

The $OP_{\text{MRC},0}^{\text{Asym}}$ in (2.40) shows that the diversity order of OPS design is $Mk_{\text{MRC}}/2$.

2.2 Downlink System Model

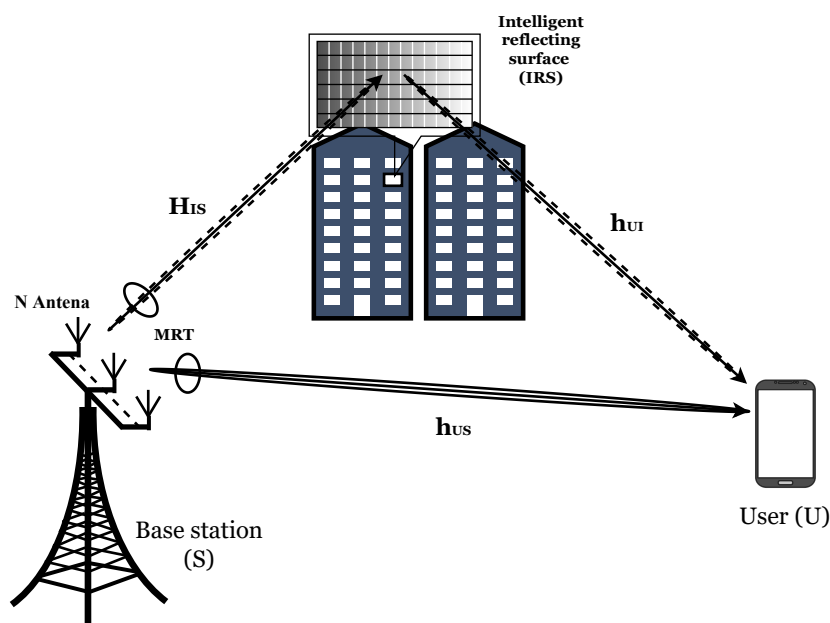


Figure 2.2: Downlink model

2.2.1 Channel Model Description

We denote the channel coefficients of the links $B \rightarrow U$ and $B \rightarrow \text{RIS}$, and $\text{RIS} \rightarrow U$ as $\mathbf{h}_{\text{BU}} = [h_{\text{BU}}^1, \dots, h_{\text{BU}}^N]$, $\mathbf{H}_{\text{BR}} = [h_{\text{BR}}^{1,1}, \dots, h_{\text{BR}}^{K,1}; \dots; h_{\text{BR}}^{1,N}, \dots, h_{\text{BR}}^{K,N}]$, and $\mathbf{h}_{\text{RU}} = [h_{\text{RU}}^1, \dots, h_{\text{RU}}^K]$, respectively. Each element of channel matrices and phase-shift configurations are considered similar to the uplink model.

In order to enhance the SNR received at the user, the B generates the vector beamforming according to two directions. In DBD, the beamforming vector is constructed as $\mathbf{w}_{\text{DBD}} = \mathbf{h}_{\text{BU}}^\dagger / \|\mathbf{h}_{\text{BU}}\|$, while for RBD, it is assembled as $\mathbf{w}_{\text{RBD}} = (\mathbf{H}_{\text{BR}}\Phi\mathbf{h}_{\text{RU}})^\dagger / \|\mathbf{H}_{\text{BR}}\Phi\mathbf{h}_{\text{RU}}\|$. Then, the B will process the RIS selection strategies as

$$p = \arg \max_{i=1,\dots,M} \|\mathbf{H}_{\text{BR}}\Phi\mathbf{h}_{\text{RU}}\|_i \mathbf{w}_{\text{DBD}} \| \quad (2.46)$$

or

$$q = \arg \max_{i=1,\dots,M} \|\mathbf{H}_{\text{BR}}\Phi\mathbf{h}_{\text{RU}}\|_i \mathbf{w}_{\text{RBD}} \| . \quad (2.47)$$

When the B employs the DBD, the received signal at the user can be expressed as

$$y_{\text{DBD}} = \left[\mathbf{h}_{\text{BU}}\mathbf{w}_{\text{DBD}} + [\mathbf{H}_{\text{BR}}\Phi\mathbf{h}_{\text{RU}}]_p \mathbf{w}_{\text{DBD}} \right] \sqrt{P}x + n. \quad (2.48)$$

Thus, the SNR received at the user with DBD to decode its own signal is given by

$$\begin{aligned} \gamma_{\text{DBD}} &= \frac{P\|\mathbf{h}_{\text{BU}}\|^2 + P\left\| [\mathbf{H}_{\text{BR}}\Phi\mathbf{h}_{\text{RU}}]_p \mathbf{w}_{\text{DBD}} \right\|^2}{\sigma^2} \\ &= \rho[\gamma_{\text{DBD1}}^2 + \gamma_{\text{DBD2}}^2], \end{aligned} \quad (2.49)$$

where $\gamma_{\text{DBD1}} = \|\mathbf{h}_{\text{BU}}\|$ and $\gamma_{\text{DBD2}} = \left\| [\mathbf{H}_{\text{BR}}\Phi\mathbf{h}_{\text{RU}}]_p \mathbf{w}_{\text{DBD}} \right\|$.

Similarly, the received signal using RBD at the B can be expressed as

$$y_{\text{RBD}} = \sqrt{P}x[\mathbf{h}_{\text{BU}}\mathbf{w}_{\text{RBD}} + [\mathbf{H}_{\text{BR}}\Phi\mathbf{h}_{\text{RU}}]_q \mathbf{w}_{\text{RBD}}] + n. \quad (2.50)$$

In this case, the SNR received for decoding the x signal at the user can be expressed

as

$$\begin{aligned}\gamma_{\text{RBD}} &= \frac{P\|\mathbf{h}_{\text{BU}}\mathbf{w}_{\text{RBD}}\|^2 + P\left\|\left[\mathbf{H}_{\text{BR}}\Phi\mathbf{h}_{\text{RU}}\right]_q\right\|^2}{\sigma^2} \\ &= \rho[\gamma_{\text{RBD1}}^2 + \gamma_{\text{RBD2}}^2],\end{aligned}\quad (2.51)$$

where $\gamma_{\text{RBD1}} = \|\mathbf{h}_{\text{BU}}\mathbf{w}_{\text{RBD}}\|$ and $\gamma_{\text{RBD2}} = \left\|\left[\mathbf{H}_{\text{BR}}\Phi\mathbf{h}_{\text{RU}}\right]_q\right\|$.

2.2.2 Outage Probability Analysis

Direct-Path Beamforming Design (DBD)

From (2.49) and outage event definitions, the OP to decode x at the user when employing DBD at the B can be expressed as

$$OP_{\text{DBD}} = \Pr(\gamma_{\text{DBD}} < \gamma_{th}). \quad (2.52)$$

Lemma 5: The closed-form expression for the OP with DBD configuration at the B and UPS alignment at the RIS can be derived as

$$OP_{\text{DBD,U}} = \frac{\Upsilon\left(N, \frac{\gamma_{th}}{\rho\Omega_{\text{UB}}}\right)}{\Gamma(N)} + \sum_{m=1}^M \frac{C_m^M (-1)^m \mu_2^{-N}}{\Omega_{\text{UB}}^N} \exp\left(-\frac{m\gamma_{th}}{\Omega_{\text{URB}}\rho}\right) \frac{\Upsilon\left(N, \frac{\mu_2\gamma_{th}}{\rho}\right)}{\Gamma(N)}, \quad (2.53)$$

where $\mu_2 = [\Omega_{\text{URB}} - m\Omega_{\text{UB}}]/[\Omega_{\text{UB}}\Omega_{\text{URB}}]$.

Proof: From (2.49), for UPS, γ_{DBD2} can be approximated to $\gamma_{\text{DBD2}} = \left\|\left[H_{\text{BR}}h_{\text{RU}}\right]_p\right\|$, and therewith, the CDF of γ_{DBD2}^2 is expressed as

$$F_{\gamma_{\text{DBD2,U}}^2} = \left[1 - \exp\left(-\frac{x}{\Omega_{\text{URB}}}\right)\right]^M. \quad (2.54)$$

From (2.49), (2.28), and (2.40), the OP of $\gamma_{\text{DBD,U}}$ can be written as

$$OP_{\text{DBD,U}} = \int_0^{\gamma_{th}/\rho} F_{\gamma_{\text{DBD2,U}}^2} \left(\frac{\gamma_{th}}{\rho} - x \right) f_{\gamma_{\text{DBD1,U}}^2}(x) dx \quad (2.55)$$

$$= \int_0^{\gamma_{th}/\rho} \left[1 - \exp \left(-\frac{\gamma_{th}}{\rho \Omega_{\text{URB}}} + \frac{x}{\Omega_{\text{URB}}} \right) \right]^M \frac{x^{N-1}}{\Gamma(N) \Omega_{\text{UB}}^N} \exp \left(-\frac{x}{\Omega_{\text{UB}}} \right) dx \quad (2.56)$$

$$= \frac{\Upsilon \left(N, \frac{x}{\Omega_{\text{UB}}} \right)}{\Gamma(N)} + \int_0^{\gamma_{th}/\rho} \sum_{m=1}^M \exp \left(-\frac{m\gamma_{th}}{\rho \Omega_{\text{URB}}} \right) \times \frac{C_m^M (-1)^m x^{N-1}}{\Gamma(N) \Omega_{\text{UB}}^N} \exp \left(x \frac{m \Omega_{\text{UB}} - \Omega_{\text{URB}}}{\Omega_{\text{URB}} \Omega_{\text{UB}}} \right) dx \quad (2.57)$$

By using [12, Eq. (3.381.1)], we can derive the expression in (2.53). The proof is completed.

Corollary 5: Similar to (2.16) and (2.25), when $\rho \rightarrow \infty$, the asymptotic of $OP_{\text{DBD,U}}$ can be expressed as

$$OP_{\text{DBD,U}}^{\text{Asym}} = \frac{[\gamma_{th}/(\rho \Omega_{\text{UB}})]^N}{N\Gamma(N)} + \sum_{m=1}^M \frac{C_m^M (-1)^m \mu_2^{-N}}{\Omega_{\text{UB}}^N} \times \frac{(\gamma_{th} \mu_2 / \rho)^N}{N\Gamma(N)} \sum_{r=0}^R \frac{[-m\gamma_{th}/(\rho \Omega_{\text{URB}})]^r}{r!}. \quad (2.58)$$

Lemma 6: The closed-form expression for the OP with DBD configuration at the B and OPS alignment at the RIS can be derived as

$$OP_{\text{DBD,O}} = \left[\frac{\Upsilon \left(k_{\text{DBD}}, \frac{\sqrt{\gamma_{th}/\rho}}{w_{\text{DBD}}} \right)}{\Gamma(k_{\text{DBD}})} \right]^M - \Xi_{\text{DBD}}, \quad (2.59)$$

where $k_{\text{DBD}} = NK\pi^3/[64 - \pi^3]$ and $w_{\text{DBD}} = (64 - \pi^3) \sqrt{\Omega_{\text{RB}} \Omega_{\text{UR}}} / [8\sqrt{N\pi^3}]$ are

the shape and scale parameters, and Ξ_{DBD} is determined as

$$\Xi_{\text{DBD}} = \frac{\gamma_{th}\pi}{\rho 2L} \sum_{l=1}^L \sqrt{1-\vartheta} \frac{\Gamma\left(N, \frac{\gamma_{th}/\rho-\eta}{\Omega_{\text{UB}}}\right)}{\Gamma(N)} f_{\gamma_{\text{DBD}2,\text{O}}^2}(\eta). \quad (2.60)$$

Proof: For OPS, $\gamma_{\text{DBD}2}$ can be approximated to

$$\gamma_{\text{DBD}2,\text{O}} = \left| \mathbf{h}_{\text{BU}}^\dagger \left[\left[\mathbf{H}_{\text{BR}} \mid \mathbf{h}_{\text{RU}} \right]_q \right] \right| / \sqrt{N\Omega_{\text{BU}}}. \quad (2.61)$$

Thus, The CDF and PDF of $\gamma_{\text{DBD}2,\text{O}}^2$ can be expressed as

$$F_{\gamma_{\text{DBD}2,\text{O}}^2}(x) = \left[\frac{\Upsilon\left(k_{\text{DBD}}, \frac{\sqrt{x}}{w_{\text{DBD}}}\right)}{\Gamma(k_{\text{DBD}})} \right]^M \quad (2.62)$$

and

$$f_{\gamma_{\text{DBD}2,\text{O}}^2}(x) = \frac{M\sqrt{x}^{k_{\text{DBD}}-2}}{2\Gamma(k_{\text{DBD}})w_{\text{DBD}}^{k_{\text{DBD}}}} \exp\left(-\frac{\sqrt{x}}{w_{\text{DBD}}}\right) \left[\frac{\Upsilon\left(k_{\text{DBD}}, \frac{\sqrt{x}}{w_{\text{DBD}}}\right)}{\Gamma(k_{\text{DBD}})} \right]^{M-1}. \quad (2.63)$$

From (2.49), (2.28), and (2.63), we can rewrite as

$$OP_{\text{DBD},\text{O}} = \int_0^{\gamma_{th}/\rho} F_{\gamma_{\text{DBD}1,\text{O}}^2}\left(\frac{\gamma_{th}}{\rho} - x\right) f_{\gamma_{\text{DBD}2,\text{O}}^2}(x) dx \quad (2.64)$$

$$= \int_0^{\gamma_{th}/\rho} \left[1 - \frac{\Gamma\left(N, \frac{\gamma_{th}/\rho-x}{\Omega_{\text{UB}}}\right)}{\Gamma(N)} \right] f_{\gamma_{\text{DBD}2,\text{O}}^2}(x) dx \quad (2.65)$$

$$= \left[\frac{\Upsilon\left(k_{\text{DBD}}, \frac{\sqrt{x}}{w_{\text{DBD}}}\right)}{\Gamma(k_{\text{DBD}})} \right]^M - \int_0^{\gamma_{th}/\rho} \frac{\Gamma\left(N, \frac{\gamma_{th}/\rho-x}{\Omega_{\text{UB}}}\right)}{\Gamma(N)} f_{\gamma_{\text{DBD}2,\text{O}}^2}(x) dx. \quad (2.66)$$

Similar to lemma 2, to overcome this hurdle, we rely on the Gaussian-Chebyshev

quadrature method, the OP of $\gamma_{\text{DBD},\text{O}}$ is obtained in (2.59). The proof is completed.

Corollary 6: Applying [12, Eq. (8.354.1)] for (2.59), when $\rho \rightarrow \infty$, the asymptotic of $OP_{\text{SC},\text{O}}$ can be expressed as

$$OP_{\text{DBD},\text{O}}^{\text{Asym}} = \left[\frac{[\gamma_{th}/(\rho w_{\text{DBD}}^2)]^{k_{\text{DBD}}/2}}{k_{\text{DBD}}\Gamma(k_{\text{DBD}})} \right]^M. \quad (2.67)$$

The $OP_{\text{DBD},\text{O}}^{\text{Asym}}$ in (2.67) shows that the diversity order of OPS design is $Mk_{\text{DBD}}/2$.

Reflective-Path Beamforming Design (RBD)

From (2.51) and outage event definitions, the OP to decode x at the user when employing RBD at the B can be expressed as

$$OP_{\text{RBD}} = \Pr(\gamma_{\text{RBD}} < \gamma_{th}). \quad (2.68)$$

Lemma 7: The closed-form expression for the OP with RBD configuration at the B and UPS alignment at the RIS can be derived as

$$OP_{\text{RBD},\text{U}} = \left[\frac{\Upsilon\left(N, \frac{\gamma_{th}}{\rho\Omega_{\text{URB}}}\right)}{\Gamma(N)} \right]^M - \exp\left(-\frac{\gamma_{th}}{\Omega_{\text{URB}}\rho}\right) \times \sum_{m=0}^{\infty} \frac{M \varepsilon(\tau_1, \tau_2, \tau_3, \tau_4) \mu_3^{-v_3}}{\Omega_{\text{URB}}^{MN} \Gamma(N)} \Upsilon\left(v_3, \frac{\mu_3\gamma_{th}}{\rho}\right), \quad (2.69)$$

where $\mu_3 = [M\Omega_{\text{UB}} - \Omega_{\text{URB}}]/[\Omega_{\text{URB}}\Omega_{\text{UB}}]$, $v_3 = MN + m$, and the entries of the recursive function $\varepsilon(\tau_1, \tau_2, \tau_3, \tau_4)$ are set as $\tau_1 = m$, $\tau_2 = M - 1$, $\tau_3 = \Omega_{\text{URB}}$, $\tau_4 = N$.

Proof: From (2.51), for uncertain phase shift, $\gamma_{\text{RBD}1}$ can be approximated to

$\gamma_{\text{RBD1,U}} = \|h_{\text{BU}}\|$. Therewith, the CDF of non-direct link as

$$F_{\gamma_{\text{RBD2,U}}^2} = 1 - \exp\left(-\frac{x}{\Omega_{\text{UB}}}\right). \quad (2.70)$$

From (2.51), the OP can be written as

$$OP_{\text{RBD,U}} = \int_0^{\gamma_{th}/\rho} F_{\gamma_{\text{RBD1,U}}^2}\left(\frac{\gamma_{th}}{\rho} - x\right) f_{\gamma_{\text{RBD2,U}}^2}(x) dx \quad (2.71)$$

$$= \int_0^{\gamma_{th}/\rho} \left[1 - \exp\left(-\frac{\gamma_{th} - x}{\Omega_{\text{UB}}}\right)\right] \frac{M x^{N-1}}{\Omega_{\text{URB}}^N \Gamma(N)} \times \exp\left(-\frac{x}{\Omega_{\text{URB}}}\right) \left[\frac{\Upsilon\left(N, \frac{x}{\Omega_{\text{URB}}}\right)}{\Gamma(N)}\right]^{M-1} dx \quad (2.72)$$

$$= \left[\frac{\Upsilon\left(N, \frac{x}{\Omega_{\text{URB}}}\right)}{\Gamma(N)}\right]^M - \int_0^{\gamma_{th}/\rho} \exp\left(-\frac{\gamma_{th}}{\rho \Omega_{\text{URB}}}\right) \times \frac{M x^{N-1}}{\Omega_{\text{URB}}^{MN} \Gamma(N)} \exp\left(-x \frac{\Omega_{\text{UB}} - \Omega_{\text{URB}}}{\Omega_{\text{URB}} \Omega_{\text{UB}}}\right) \left[\sum_{m=0}^{\infty} \frac{x^m}{\Omega_{\text{URB}}^m \Gamma(N)}\right]^{M-1} dx \quad (2.73)$$

$$= \left[\frac{\Upsilon\left(N, \frac{x}{\Omega_{\text{URB}}}\right)}{\Gamma(N)}\right]^M - \int_0^{\gamma_{th}/\rho} \exp\left(-\frac{\gamma_{th}}{\rho \Omega_{\text{URB}}}\right) \times \frac{M x^{N-1}}{\Omega_{\text{URB}}^{MN} \Gamma(N)} \exp\left(-x \frac{\Omega_{\text{UB}} - \Omega_{\text{URB}}}{\Omega_{\text{URB}} \Omega_{\text{UB}}}\right) \sum_{m=0}^{\infty} \varepsilon(\tau_1, \tau_2, \tau_3, \tau_4) x^{MN+m-1} dx. \quad (2.74)$$

By using [12, Eq. (3.381.1)], we can achieve the closed-form expression as in (2.69). The proof is completed.

Corollary 7: Applying (2.16) and (2.25) for (2.69), when $\rho \rightarrow \infty$, the asymptotic of $OP_{\text{SC,O}}$ can be expressed as

$$\begin{aligned}
OP_{\text{RBD,U}}^{\text{Asym}} &= \left[\frac{[\gamma_{th}/(\rho\Omega_{\text{URB}})]^N}{N\Gamma(N)} \right]^M - \sum_{r=0}^R \frac{[-\gamma_{th}/(\rho\Omega_{\text{UB}})]^r}{r!} \\
&\times \frac{[\gamma_{th}\mu_3/\rho]^{v_3}}{v_3\Gamma(v_3)} \frac{\sum_{m=0}^{\infty} \varepsilon(\tau_1, \tau_2, \tau_3, \tau_4) M \mu_3^{-v_3}}{\Omega_{\text{URB}}\Gamma(N)}. \tag{2.75}
\end{aligned}$$

Remark 2: Similar to Remark 1, we provide the ratio of $OP_{\text{RBD,U}}^{\text{Ana}}/OP_{\text{RBD,U}}^{\text{Sim}}$ to consider the convergence of (2.75).

Lemma 8: The closed-form expression for the OP with RBD configuration at the B and OPS alignment at the RIS can be derived as

$$OP_{\text{RBD,O}} = \left[\frac{\Upsilon \left(k_{\text{RBD2}}, \frac{\sqrt{\gamma_{th}/\rho}}{w_{\text{RBD2}}} \right)}{\Gamma(k_{\text{RBD2}})} \right]^M - \Xi_{\text{RBD}}, \tag{2.76}$$

where $k_{\text{RBD2}} = NK\pi^2/[16 - \pi^2]$, $w_{\text{RBD2}} = (16 - \pi^2) \sqrt{\Omega_{\text{RB}}\Omega_{\text{UR}}}/[4\pi]$ are the shape and scale parameters, and Ξ_{RBD} is determined as

$$\Xi_{\text{RBD}} = \frac{\gamma_{th}\pi}{\rho 2L} \sum_{l=1}^L \sqrt{1 - \vartheta} \frac{\Gamma \left(k_{\text{RBD1}}, \frac{\sqrt{\eta}}{w_{\text{RBD1}}} \right)}{\Gamma(k_{\text{RBD1}})} f_{\gamma_{\text{RBD2,O}}^2}(\eta), \tag{2.77}$$

where $\eta = \gamma_{th}N(\vartheta + 1)/(2\rho)$. $k_{\text{RBD1}} = N\pi/[4 - \pi]$ and $w_{\text{RBD1}} = (4 - \pi) \sqrt{\Omega_{\text{UB}}}/[2\sqrt{\pi}]$ are the shape and scale parameters.

Proof: From (2.51), for OPS, γ_{RBD1} can be approximated to $\gamma_{\text{RBD1,O}} = \left\| \sqrt{N} |h_{\text{BU}}| \right\|$. Thus, the CDF and PDF of direct link can be expressed as

$$F_{\gamma_{\text{RBD1,O}}^2}(x) = \left[\frac{\Upsilon \left(k_{\text{RBD1}}, \frac{\sqrt{x}}{w_{\text{RBD1}}} \right)}{\Gamma(k_{\text{RBD1}})} \right] \tag{2.78}$$

and

$$f_{\gamma_{\text{RBD1},\text{O}}^2}(x) = \frac{M\sqrt{x}^{k_{\text{RBD1}}-2}}{2\Gamma(k_{\text{RBD1}})w_{\text{RBD1}}^{k_{\text{RBD1}}}} \exp\left(-\frac{\sqrt{x}}{w_{\text{RBD1}}}\right). \quad (2.79)$$

The CDF and PDF of $\gamma_{\text{RBD2},\text{O}}^2$ can be expressed as

$$F_{\gamma_{\text{RBD2},\text{O}}^2}(x) = \left[\frac{\Upsilon\left(k_{\text{RBD2}}, \frac{\sqrt{x}}{w_{\text{RBD2}}}\right)}{\Gamma(k_{\text{RBD2}})} \right]^M \quad (2.80)$$

and

$$f_{\gamma_{\text{RBD2},\text{O}}^2}(x) = \frac{M\sqrt{x}^{k_{\text{RBD2}}-2}}{2w_{\text{RBD2}}^{k_{\text{RBD2}}}\Gamma(k_{\text{RBD2}})} \exp\left(-\frac{\sqrt{x}}{w_{\text{RBD2}}}\right) \left[\frac{\Upsilon\left(k_{\text{RBD2}}, \frac{\sqrt{x}}{w_{\text{RBD2}}}\right)}{\Gamma(k_{\text{RBD2}})} \right]^{M-1}. \quad (2.81)$$

From (2.51), (2.78), and (2.80), the OP can be written as

$$OP_{\text{RBD},\text{O}} = \int_0^{N\gamma_{\text{th}}/\rho} F_{\gamma_{\text{RBD1},\text{O}}^2}\left(\frac{N\gamma_{\text{th}}}{\rho} - x\right) f_{\gamma_{\text{RBD2},\text{O}}^2}(x) dx \quad (2.82)$$

$$= \int_0^{N\gamma_{\text{th}}/\rho} \left[1 - \frac{\Gamma\left(k_{\text{RBD1}}, \frac{\sqrt{x}}{w_{\text{RBD1}}}\right)}{\Gamma(k_{\text{RBD1}})} \right] f_{\gamma_{\text{RBD2},\text{O}}^2} dx \quad (2.83)$$

$$= \left[\frac{\Upsilon\left(k_{\text{RBD2}}, \frac{\sqrt{x}}{w_{\text{RBD2}}}\right)}{\Gamma(k_{\text{RBD2}})} \right]^M - \int_0^{N\gamma_{\text{th}}/\rho} \frac{\Gamma\left(k_{\text{RBD1}}, \frac{\sqrt{N\gamma_{\text{th}}/\rho - x}}{w_{\text{RBD1}}}\right)}{\Gamma(k_{\text{RBD1}})} f_{\gamma_{\text{RBD2},\text{O}}^2} dx. \quad (2.84)$$

Similar to lemma 2, to overcome this hurdle, we rely on the Gaussian-Chebyshev quadrature method. The OP of $\gamma_{\text{RBD},\text{O}}$ is obtained in (2.77). The proof is completed.

Corollary 8: Applying [12, Eq. (8.354.1)] for (2.77), the asymptotic of $OP_{\text{RBD},\text{O}}$

can be expressed as

$$OP_{\text{RBD,O}}^{\text{Asym}} = \left[\frac{[\gamma_{th}/(\rho w_{\text{RBD2}}^2)]^{k_{\text{RBD2}}/2}}{k_{\text{RBD2}}\Gamma(k_{\text{RBD2}})} \right]^M. \quad (2.85)$$

The $OP_{\text{RBD,O}}^{\text{Asym}}$ in (2.85) shows that the diversity order of OPS design is $Mk_{\text{RBD2}}/2$.

Chapter 3

Results and Discussion

In this section, we use Monte-Carlo simulations to show the OP tendency of the considered system and to verify the accuracy of the theoretical analysis derived in Sec. III. All parameters used for simulation are listed in Table. 3.1. Taking into account the effect of path-loss, we set $\Omega_{AC} = d_{AC}^{-PL}$, where d_{AC} denote the physical distance between A and C while PL is the related path-loss exponent. Additionally, we label analysis and simulation results as “Ana.” and “Sim.”, respectively.

Table 3.1: Parameters and values for analysis and simulation.

Parameters	Value
Location of B	(0, 0)
Location of RIS	(35, 35)
Location of U	(10, 60)
Path-loss exponent, PL	3
Noise variance, σ^2	1
Monte-Carlo sample	10^6
Gaussian-Chebyshev sample, L	30

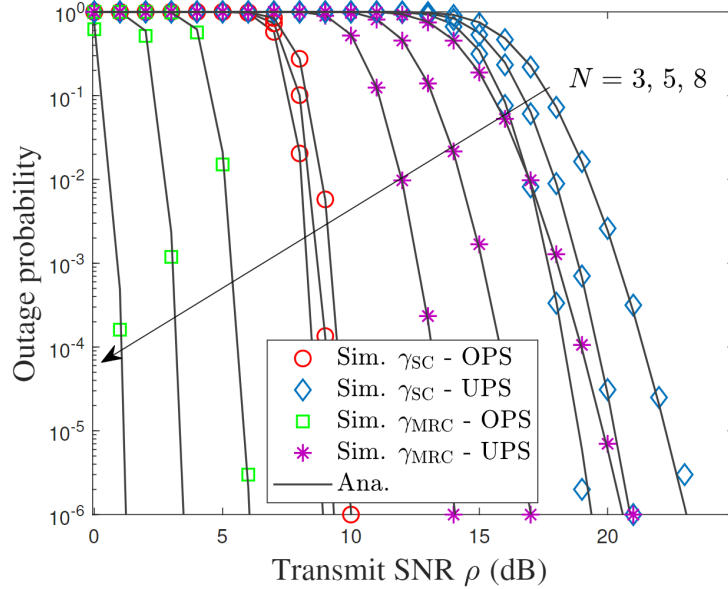


Figure 3.1: Effects of N on the OP of B with $M = 5$ and $K = 30$.

3.1 Uplink Model

In Fig. 3.1, we depict the OP at the B versus transmit SNR (in dB) under different antenna configurations. It is observed clearly that the simulation results coincide with those of the theoretical analysis, verifying the accuracy of Lemmas 1 to 4. From Fig. 3.1, it can be observed that when MRC technique is used at B, the OP dramatically decreases with the increment of the SNRs as well as the number of antenna settings. In particular, to satisfy the $OP = 10^{-5}$, OPS needs the increment of SNR up to 5 dB in the case of $N = 3$ and 2 dB in the case of $N = 8$. Meanwhile, UPS is required to increase the SNR up to 20 dB in the case of $N = 3$ and 14 dB in the case of $N = 8$. By comparing the OP with UPS and OPS, some interesting observations are recognized as: (i) The system with MRC can save a significant amount of budgeted transmit power (i.e., represented by SNR) around 12dB and 15 dB when deploying OPS. (ii) The OP tends to decrease with the increase of N . (iii) By doubling antenna settings, the system achieves

approximately 2.5 dB improvement. Regarding the case of B using SC, it is also observed that the OP with OPS is always better than that of UPS, and it only requires a transmit power up to 9-10 dB to ensure the OP requirement with 10^{-5} , whereas the UPS need to request the transmit power up to 18-23 dB. Moreover, the figure also reveals that the OP with OPS is less sensitive with the increase of N while the OP with UPS is strongly affected by N . Evidently, when N increases from 3 to 8, the transmit power corresponding to the OP curves with OPS only decreases 1 dB while that of the OP with UPS decreases 5 dB. Next, the figure shows that the OP curves with MRC outperform those with SC in both UPS and OPS. For example, when using the OPS, the MRC achieves 4 dB and 8 dB gain for $N = 3$ and $N = 8$, respectively, in comparison with SC. For the case of UPS, the MRC also obtains 2 dB and 5 dB gain for $N = 3$ and $N = 8$ with respect to SC. This is because the MRC technique produces maximum SNR by combining all the signals from the antennas, while the SC technique only selects an antenna with the best SNR received. Although MRC outperforms the performance when compared to SC, it should be noted that MRC required complex hardware implementation and higher costs. Furthermore, we should also note that using MRC is not always better than SC. Specifically, we can easily observe from the figure that MRC with UPS has lower OP than SC with OPS. Therefore, for a system requiring low-cost implementation and low-complexity design, SC with OPS can become a promising solution.

Next, we focus on evaluating the impact of the number of distributed RISs in Fig. 3.2. Similar to the observation in Fig. 3.1, the OP with MRC achieves superior performance than that of SC in both UPS and OPS. It can be observed that when M increases from 3 to 8, the OP with OPS only decreases slightly, while the OP with UPS tends to decrease significantly. Clearly, the transmit power for the OPS has 1 dB improvement, while that of the UPS attains 2.5 dB enhancement.

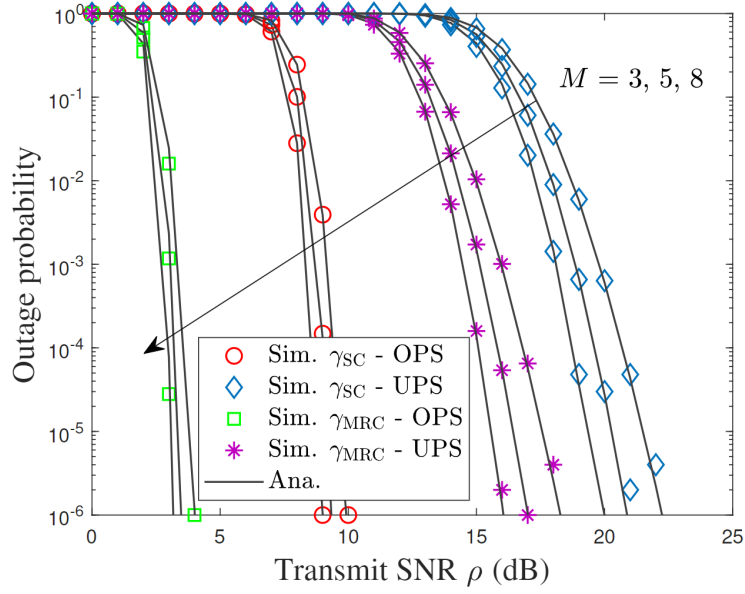


Figure 3.2: Effects of M on the OP of B with $N = 5$ and $K = 30$.

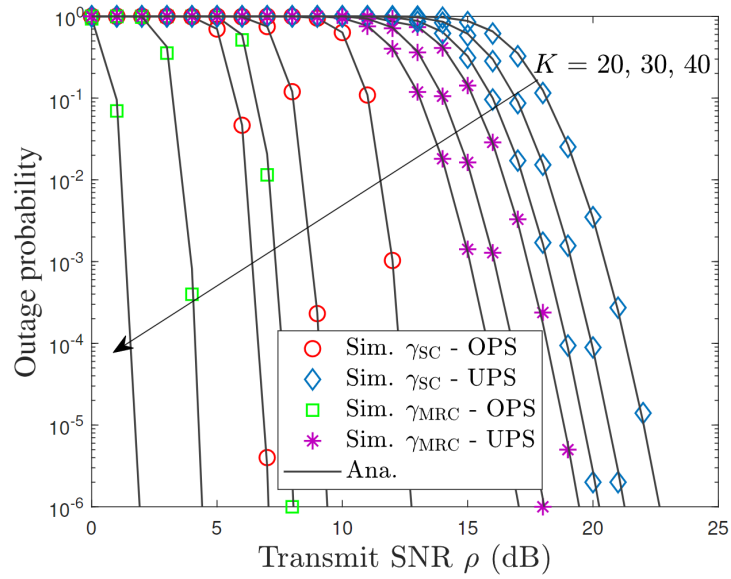


Figure 3.3: Effects of the number of the reflector at RIS on the OP of B when $M = 6$ and $N = 4$.

To capture the effect of reflective configuration at RIS, we plot the OP with the increase of K in Fig. 3.3. As K increases from 20 to 30 as well as from 30 to 40,

the OP with UPS maintains the performance gap improvement of 1 dB, while that of OPS earns 2.5 dB. This means that when increasing the number of units per each RIS array up to 10 units, the system with OPS can save approximately half of the transmit power budget, showing the advantage of RIS for the uplink scenario in future deployments, especially for low-cost mobile devices. Besides, from the results of Figs. 3.1 and 3.3, we can see that the performance gap of MRC-OPS when K increases from 20 to 40 is slightly better than when N increases from 3 to 8. In the case of SC-OPS, the increase of K provide outstanding performance of the OP when compared to the increase of N . Meanwhile, in the UPS scenarios, increasing N shows a better reduction of OP than increasing K .

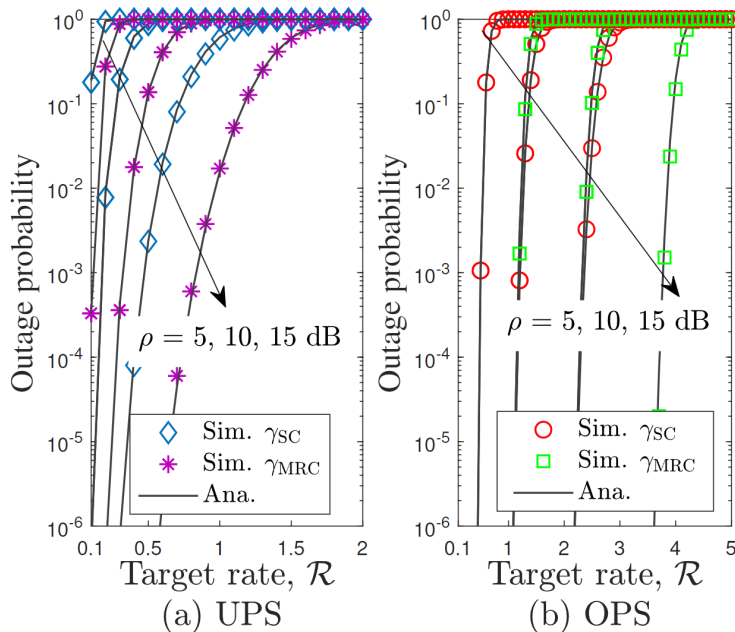


Figure 3.4: Effects of SNR (dB) on the OP of B with $M = 6$, $N = 4$, and $K = 30$.

Finally, in Fig. 3.4, we assess the impact of SNRs for the uplink transmission on the outage performance. As the SNR is fixed at 5dB, the OP curves with UPS in Fig. 5(a) tend to increase quickly as the target data rate transmission increases from 0.1 bit/s/Hz to 0.15 bit/s/Hz and then saturate the convergence at 1 for

the rest. This means that the user only transmits low target data rate. When the user wants to send data with a high data rate transmission, the system has to consume much more energy and requires better signal improvement. Clearly, as the data rate demands on 1 bit/s/Hz with $OP = 10^{-2}$, the MRC should be configured at B and the user's transmit power requirement is set up to 15 dB. However, by employing the OPS in Fig. 5(b), the user only needs 5 dB with SC configurations to achieve the same condition. Interestingly, when the SNR is fixed at 15dB, the target data rate for OPS can be greatly increased up to 2 bit/s/Hz for SC and 4 bit/s/Hz for MRC. Moreover, from the figure, we can see that the rate performance gap between using MRC and SC increases as the increment of SNR. Specifically, in Fig. 5(a), when the SNR increases from 5 dB to 15 dB and considering $OP = 10^{-4}$, the rate performance gap for UPS will increase from 0.1 to 0.4. Meanwhile, in Fig. 5(b), the rate performance for OPS will increase from 0.8 to 1.2.

3.2 Downlink Model

In Fig. 3.5, we compare the performance of using DBD and RBD at the B for downlink transmission scenarios. In particular, we present the analytical and simulated OP against the average SNR under varying transmitter antenna settings. Besides, two different kinds of phase-shift design at RIS, namely UPS and OPS, are also provided for comparison. Similar to uplink results, the analytical results agree with the simulation ones. Moreover, there are three important observations: (1) The outage performance improves with the increment of N . This is because the higher antenna setting leads to increasing vector beamforming gain for the SNR received for the user. (2) Using RBD provides better performance over 1 dB and approximately 2.5 dB than that of DBD in the cases of OPS and UPS,

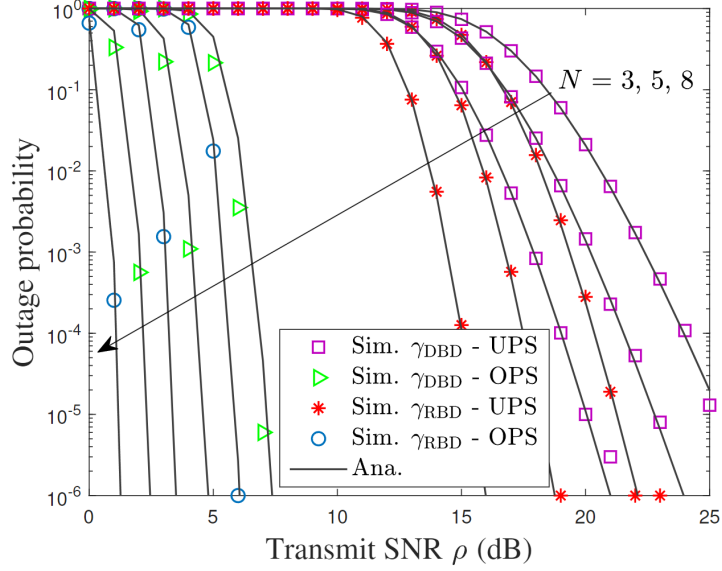


Figure 3.5: Effects of N on the OP of U with $M = 5$ and $K = 30$.

respectively. Here, the main reason for this case is that when configuring DBD, the user receives two streams of signal enhancement; thus, the received SNR is maximized. Meanwhile, using RBD only strengthens the stream incident signals to RIS without enhancing the reflecting signal from RIS to the user, resulting in fewer improvements. (3) Compared with UPS, using the OPS setting can save the budget to transmit SNR up to more than 12 dB for large OP (i.e., $OP > 10^{-2}$); however, this gap will increase for smaller OP expectation. For example, when $OP = 10^{-4}$, the gap between DBD with OPS and UPS is 17 dB and the gap between RBD with OPS and UPS is 15 dB.

In Fig. 3.6, we evaluate the impact of the number of RIS-distributed on the performance of the user. It can be intuitively observed that increasing M does not provide performance improvement for OPS but achieves a significant performance enhancement for UPS. Clearly, to satisfy the $OP = 10^{-5}$ when M increases from 3 to 8, the OP curves with OPS only improve 1 dB, while in the case of UPS, the OP improves approximately 3 dB. The main reason for this tendency can be explained

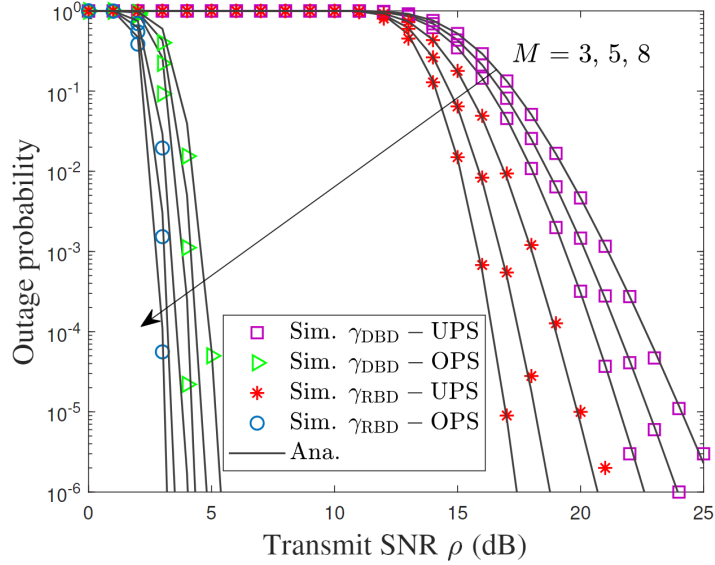


Figure 3.6: Effects of M on the OP of U with $N = 5$ and $K = 30$.

as follows. Most distributed RISs using OPS are constructed to maximize the channel gain from B to the user via phase-shift alignment, yielding very small performance gap between RISs. Meanwhile, for UPS deployments, selecting the best RIS provides great enhancement since this method can help us find out the best phase-shift alignment at RIS.

In Fig. 3.7, we examine the effect of the number of implemented reflectors on the optimal RIS. The results show that when K increases, the outage performance decreases significantly. In particular, when the number of reflectors increases from 20 to 30 and from 30 to 40, there exists a performance gap improvement for OPS and UPS. Specifically, the performance gap with UPS is 1 dB, which is similar to the case of uplink transmission. However, the performance gap with OPS is 4dB, which is better by 1.5 dB compared to uplink transmission. Additionally, for OPS scenarios, increasing K in Fig. 3.7 provides a slightly better OP performance than increasing N in Fig. 3.5, while for the UPS scenario, increasing the number of antennas provides better performance than increasing K . Therefore, we can

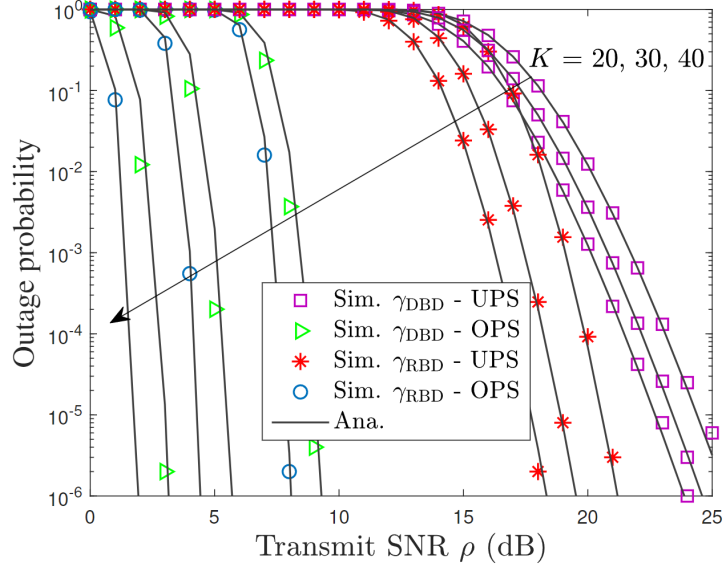


Figure 3.7: Effects of the number of reflectors at RIS on the OP of U with $M = 6$ and $N = 4$.

deduce that the large element RIS can provide better performance for the OPS scenarios than the B with multiple antennas. Meanwhile, for the UPS scenarios, multiple antennas at B will show greater performance when compared to large RISs. Therefore, combined with Fig. 3.6, the selection RIS can help UPS improve OP performance with large RISs.

In Fig. 3.8, we show the impact of the SNRs on the user's outage performance. The figure shows that the analytical results match the simulated ones. As expected, it is found that the OP increases with the increase of data rate transmission and OPS alignment provides better data rate transmission than UPS. In addition, the results also show that increasing transmitting SNR results in significant OP improvement as well as increasing the performance gap between using DBD and RBD. In particular, as SNR increases from 5 dB to 15 dB, the performance gap with UPS only increases 0.4 bit/z/Hz, whereas that of OPS increases approximately up to 2.5 bit/s/Hz.

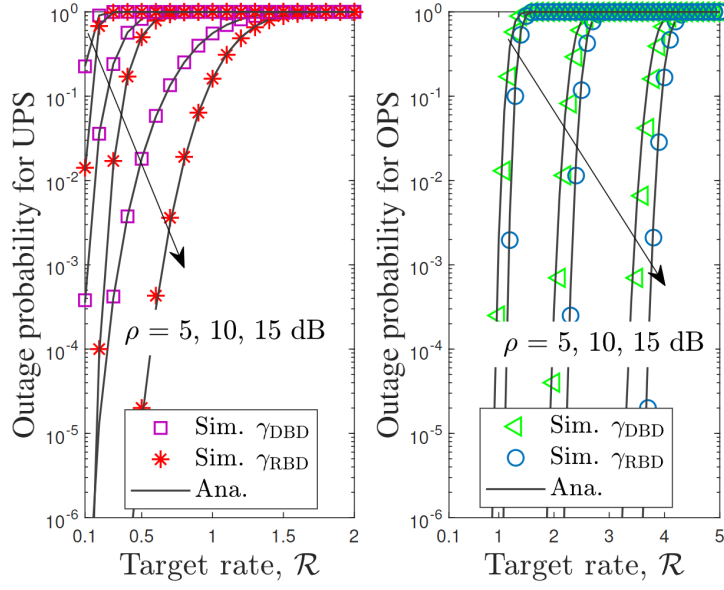


Figure 3.8: Effects of SNR (dB) on the OP of U with $M = 6$, $N = 4$, and $K = 30$.

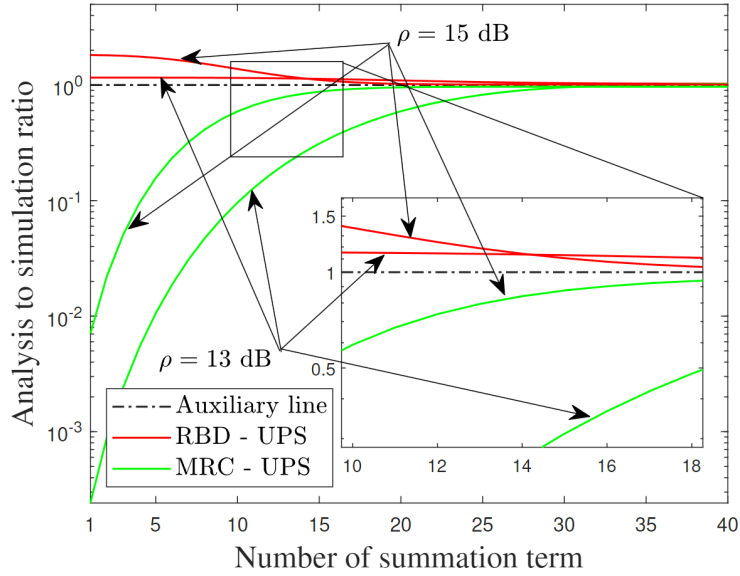


Figure 3.9: The effects of the number of summation terms on closed-form expressions with $M = 6$, $N = 4$, and $K = 30$.

Finally, to show the convergence of infinite series involving the derived analysis in Lemmas 3 and 7, we plot the ratio between the analysis and simulation results

versus the number of summation terms under varying SNR settings. As can be observed, the ratio curves tend to converge to the auxiliary line as the number of used terms increases. Aside from that, at $\rho = 13$ dB, the gap between the ratio RDB curve and the auxiliary one is relatively small compared to that of MRC. However, this case requires at least 30 terms to be converged. Interestingly, when ρ increases from 13 to 15 dB, the number of used terms tends to reduce. Exceptionally, using only 20 terms is sufficient for RDB and MRC to get the convergence. Therefore, we can conclude that the number of used terms primarily depends on the considered SNR values. For example, if a system is operating at a low or medium SNR regime, the number of used terms must be large; otherwise, a small number of terms is sufficient.

Chapter 4

Conclusions

This thesis has investigated the performance of uplink/downlink RIS-based wireless systems over Rayleigh fading channels. To enhance the system performance, we focused on three aspects: (1) the phase-shift alignment at RISs, (2) antenna configurations at B, and (3) the RIS selection strategies. Accordingly, we provided extensive simulation results to validate the theoretical analysis results. Numerical results revealed that: In both uplink and downlink transmission with the OPS scenario, the RISs equipped with a large number of elements provide more benefits than configuring multiple antennas at B. Meanwhile, using selection RIS can overcome the performance disadvantage in the UPS scenario. Additionally, for uplink transmissions, employing OPS alignment always provides better OP performance than UPS. Adopting MRC always shows better OP compared to the SC in the same scenario, while the SC-OPS presents better OP performance than MRC-UPS. For downlink transmissions, the results showed that: (i) Using RBD provides better OP than using DBD in both OPS and RPS; (ii) The OPS scenario achieves 13 dB better OP performance than the UPS regardless of applying DBD or RBD; and (iii) When increasing the number of distributed IRSs, the OP of the UPS is significantly reduced compared to that of OPS.

List of Publications

SCI(E) Journals

- [R1] Khac-Tuan Nguyen, Thai-Hoc Vu, and Sunghwan Kim. “Exploiting reconfigurable intelligent surface-based uplink/downlink wireless systems”. *IEEE Access*, 10:91059–91072, 2022.
- [R2] Khac-Tuan Nguyen, Thai-Hoc Vu, and Sunghwan Kim. “Performance analysis and deep learning design of short-packet communication in multi-RIS aided multi-antenna wireless systems”. Accepted to *IEEE Internet of Things Journal*.
- [R3] Khac-Tuan Nguyen, Thai-Hoc Vu, and Sunghwan Kim. “A unified framework analysis for reconfigurable intelligent surface-aided coordinated NOMA systems”. Accepted to *IEEE Transactions on Vehicular Technology*.

International Conferences

- [R4] Khac-Tuan Nguyen, Thai-Hoc Vu, Thi-Huong Khuat, Hai-Chau Le, and Sunghwan Kim. “Performance analysis of uplink MISO systems with RIS selections and MRC/SC configurations”. In *2022 IEEE Ninth International Conference on Communications and Electronics (ICCE)*, pages 145–148, 2022.
- [R5] Thai-Hoc Vu, Khac-Tuan Nguyen, Quoc-Viet Pham, Thien Huynh-The, Daniel Benevides da Costa, Vo Nguyen Quoc Bao, and Sunghwan Kim. “Outage performance of THz-aided NOMA systems with spherical stochastic model”. Accepted to *2023 IEEE Statistical Signal Processing (SSP) Workshop*.

Bibliography

- [1] Samith Abeywickrama, Rui Zhang, Qingqing Wu, and Chau Yuen. Intelligent reflecting surface: Practical phase shift model and beamforming optimization. *IEEE Transactions on Communications*, 68(9):5849–5863, 2020.
- [2] Bayan Al-Nahhas, Qurrat-Ul-Ain Nadeem, and Anas Chaaban. Reconfigurable intelligent surface aided communications: Asymptotic analysis under imperfect csi. *arXiv preprint arXiv:2108.09388*, 2021.
- [3] Ertugrul Basar. Reconfigurable intelligent surface-based index modulation: A new beyond mimo paradigm for 6g. *IEEE Transactions on Communications*, 68(5):3187–3196, 2020.
- [4] Emil Björnson, Özgecan Özdogan, and Erik G Larsson. Intelligent reflecting surface versus decode-and-forward: How large surfaces are needed to beat relaying? *IEEE Wireless Communications Letters*, 9(2):244–248, 2019.
- [5] Emil Björnson, Luca Sanguinetti, Henk Wymeersch, Jakob Hoydis, and Thomas L Marzetta. Massive mimo is a reality—what is next?: Five promising research directions for antenna arrays. *Digital Signal Processing*, 94:3–20, 2019.

- [6] Alexandros-Apostolos A Boulogeorgos and Angeliki Alexiou. Performance analysis of reconfigurable intelligent surface-assisted wireless systems and comparison with relaying. *IEEE Access*, 8:94463–94483, 2020.
- [7] Lalit Chettri and Rabindranath Bera. A comprehensive survey on internet of things (iot) toward 5g wireless systems. *IEEE Internet of Things Journal*, 7(1):16–32, 2020.
- [8] Tie Jun Cui, Mei Qing Qi, Xiang Wan, Jie Zhao, and Qiang Cheng. Coding metamaterials, digital metamaterials and programmable metamaterials. *Light: science & applications*, 3(10):e218–e218, 2014.
- [9] Boya Di, Hongliang Zhang, Lingyang Song, Yonghui Li, Zhu Han, and H Vincent Poor. Hybrid beamforming for reconfigurable intelligent surface based multi-user communications: Achievable rates with limited discrete phase shifts. *IEEE Journal on Selected Areas in Communications*, 38(8):1809–1822, 2020.
- [10] Marco Di Renzo, Konstantinos Ntontin, Jian Song, Fadil H Danufane, Xuewen Qian, Fotis Lazarakis, Julien De Rosny, Dinh-Thuy Phan-Huy, Osvaldo Simeone, Rui Zhang, et al. Reconfigurable intelligent surfaces vs. relaying: Differences, similarities, and performance comparison. *IEEE Open Journal of the Communications Society*, 1:798–807, 2020.
- [11] Limeng Dong and Hui-Ming Wang. Secure mimo transmission via intelligent reflecting surface. *IEEE Wireless Communications Letters*, 9(6):787–790, 2020.
- [12] Izrail Solomonovich Gradshteyn and Iosif Moiseevich Ryzhik. *Table of integrals, series, and products*. Academic press, 2014.

- [13] Chang Guo, Ying Cui, Feng Yang, and Lianghai Ding. Outage probability analysis and minimization in intelligent reflecting surface-assisted miso systems. *IEEE Communications Letters*, 24(7):1563–1567, 2020.
- [14] Yu Han, Wankai Tang, Shi Jin, Chao-Kai Wen, and Xiaoli Ma. Large intelligent surface-assisted wireless communication exploiting statistical csi. *IEEE Transactions on Vehicular Technology*, 68(8):8238–8242, 2019.
- [15] Sha Hu, Fredrik Rusek, and Ove Edfors. Beyond massive mimo: The potential of data transmission with large intelligent surfaces. *IEEE Transactions on Signal Processing*, 66(10):2746–2758, 2018.
- [16] Chongwen Huang, Alessio Zappone, George C Alexandropoulos, Mérouane Debbah, and Chau Yuen. Reconfigurable intelligent surfaces for energy efficiency in wireless communication. *IEEE Transactions on Wireless Communications*, 18(8):4157–4170, 2019.
- [17] Abla Kammoun, Anas Chaaban, Mérouane Debbah, Mohamed-Slim Alouini, et al. Asymptotic max-min sinr analysis of reconfigurable intelligent surface assisted miso systems. *IEEE Transactions on Wireless Communications*, 19(12):7748–7764, 2020.
- [18] Aymen Khaleel and Ertugrul Basar. Reconfigurable intelligent surface-empowered mimo systems. *IEEE Systems Journal*, 15(3):4358–4366, 2020.
- [19] Neel Kanth Kundu and Matthew R McKay. Ris-assisted miso communication: Optimal beamformers and performance analysis. In *2020 IEEE Globecom Workshops (GC Wkshps*, pages 1–6. IEEE, 2020.
- [20] Christos Liaskos, Shuai Nie, Ageliki Tsioliaridou, Andreas Pitsillides, Sotiris Ioannidis, and Ian Akyildiz. A new wireless communication paradigm

- through software-controlled metasurfaces. *IEEE Communications Magazine*, 56(9):162–169, 2018.
- [21] Yang Liu, Jun Zhao, Ming Li, and Qingqing Wu. Intelligent reflecting surface aided miso uplink communication network: Feasibility and power minimization for perfect and imperfect csi. *IEEE Transactions on Communications*, 69(3):1975–1989, 2020.
- [22] Yuanwei Liu, Xiao Liu, Xidong Mu, Tianwei Hou, Jiaqi Xu, Marco Di Renzo, and Naofal Al-Dhahir. Reconfigurable intelligent surfaces: Principles and opportunities. *IEEE Communications Surveys & Tutorials*, 23(3):1546–1577, 2021.
- [23] Yuanwei Liu, Xiao Liu, Xidong Mu, Tianwei Hou, Jiaqi Xu, Marco Di Renzo, and Naofal Al-Dhahir. Reconfigurable intelligent surfaces: Principles and opportunities. *IEEE communications surveys & tutorials*, 23(3):1546–1577, 2021.
- [24] Abubakar U Makarfi, Rupak Kharel, Khaled M Rabie, Omprakash Kaiwartya, Xingwang Li, and Dinh-Thuan Do. Reconfigurable intelligent surfaces based cognitive radio networks. In *2021 IEEE Wireless Communications and Networking Conference Workshops (WCNCW)*, pages 1–6. IEEE, 2021.
- [25] Abubakar U Makarfi, Khaled M Rabie, Omprakash Kaiwartya, Osamah S Badarneh, Xingwang Li, and Rupak Kharel. Reconfigurable intelligent surface enabled iot networks in generalized fading channels. In *ICC 2020-2020 IEEE International Conference on Communications (ICC)*, pages 1–6. IEEE, 2020.
- [26] Jawad Mirza, Bakhtiar Ali, and Muhammad Awais Javed. Stable matching for selection of intelligent reflecting surfaces in multiuser miso systems. *IEEE Communications Letters*, 25(8):2748–2752, 2021.

- [27] Khac-Tuan Nguyen, Thai-Hoc Vu, Thi-Huong Khuat, Hai-Chau Le, and Sunghwan Kim. Performance analysis of uplink miso systems with ris selections and mrc/sc configurations. In *2022 IEEE Ninth International Conference on Communications and Electronics (ICCE)*, pages 145–148, 2022.
- [28] Khac-Tuan Nguyen, Thai-Hoc Vu, and Sunghwan Kim. Exploiting reconfigurable intelligent surface-based uplink/downlink wireless systems. *IEEE Access*, 10:91059–91072, 2022.
- [29] Thi-Mien Nguyen, Linh T Nguyen, Khac-Tuan Nguyen, and Hai-Chau Le. Performance analysis of short-packet communications in multi-ris-based uplink systems. In *Proceedings of the 11th International Symposium on Information and Communication Technology*, pages 180–185, 2022.
- [30] Mohanad Obeed and Anas Chaaban. Relay–reconfigurable intelligent surface cooperation for energy-efficient multiuser systems. In *2021 IEEE International Conference on Communications Workshops (ICC Workshops)*, pages 1–6. IEEE, 2021.
- [31] Cunhua Pan, Hong Ren, Kezhi Wang, Jonas Florentin Kolb, Maged Elkashlan, Ming Chen, Marco Di Renzo, Yang Hao, Jiangzhou Wang, A. Lee Swindlehurst, Xiaohu You, and Lajos Hanzo. Reconfigurable intelligent surfaces for 6g systems: Principles, applications, and research directions. *IEEE Communications Magazine*, 59(6):14–20, 2021.
- [32] Cunhua Pan, Hong Ren, Kezhi Wang, Wei Xu, Maged Elkashlan, Arumugam Nallanathan, and Lajos Hanzo. Multicell mimo communications relying on intelligent reflecting surfaces. *IEEE Transactions on Wireless Communications*, 19(8):5218–5233, 2020.

- [33] Pulasthi P Perera, Vanodhya G Warnasooriya, Dhanushka Kudathanthirige, and Himel A Suraweera. Sum rate maximization in star-ris assisted full-duplex communication systems. In *ICC 2022-IEEE International Conference on Communications*, pages 3281–3286. IEEE, 2022.
- [34] Marco Di Renzo, Merouane Debbah, Dinh-Thuy Phan-Huy, Alessio Zappone, Mohamed-Slim Alouini, Chau Yuen, Vincenzo Sciancalepore, George C Alexandropoulos, Jakob Hoydis, Haris Gacanin, et al. Smart radio environments empowered by reconfigurable ai meta-surfaces: An idea whose time has come. *EURASIP Journal on Wireless Communications and Networking*, 2019(1):1–20, 2019.
- [35] José David Vega Sánchez, Pablo Ramirez-Espinosa, and F Javier López-Martínez. Physical layer security of large reflecting surface aided communications with phase errors. *IEEE Wireless Communications Letters*, 10(2):325–329, 2020.
- [36] N. Rajatheva *et al.* White paper on broadband connectivity in 6g. 2022.
- [37] Trinh Van Chien, Lam Thanh Tu, Symeon Chatzinotas, and Björn Ottersten. Coverage probability and ergodic capacity of intelligent reflecting surface-enhanced communication systems. *IEEE Communications Letters*, 25(1):69–73, 2020.
- [38] Thai-Hoc Vu, Toan-Van Nguyen, Daniel Benevides da Costa, and Sunghwan Kim. Intelligent reflecting surface-aided short-packet non-orthogonal multiple access systems. *IEEE Transactions on Vehicular Technology*, 71(4):4500–4505, 2022.

- [39] Thai-Hoc Vu, Toan-Van Nguyen, and Sunghwan Kim. Cooperative noma-enabled swipt iot networks with imperfect sic: Performance analysis and deep learning evaluation. *IEEE Internet of Things Journal*, 9(3):2253–2266, 2022.
- [40] Qingqing Wu and Rui Zhang. Intelligent reflecting surface enhanced wireless network via joint active and passive beamforming. *IEEE Transactions on Wireless Communications*, 18(11):5394–5409, 2019.
- [41] Qingqing Wu, Shuowen Zhang, Beixiong Zheng, Changsheng You, and Rui Zhang. Intelligent reflecting surface-aided wireless communications: A tutorial. *IEEE Transactions on Communications*, 69(5):3313–3351, 2021.
- [42] Lei Zhang, Cunhua Pan, Yu Wang, Hong Ren, and Kezhi Wang. Robust beamforming design for intelligent reflecting surface aided cognitive radio systems with imperfect cascaded csi. *IEEE Transactions on Cognitive Communications and Networking*, 8(1):186–201, 2021.
- [43] Shuowen Zhang and Rui Zhang. Capacity characterization for intelligent reflecting surface aided mimo communication. *IEEE Journal on Selected Areas in Communications*, 38(8):1823–1838, 2020.
- [44] Kangda Zhi, Cunhua Pan, Hong Ren, and Kezhi Wang. Uplink achievable rate of intelligent reflecting surface-aided millimeter-wave communications with low-resolution adc and phase noise. *IEEE Wireless Communications Letters*, 10(3):654–658, 2020.
- [45] Gui Zhou, Cunhua Pan, Hong Ren, Kezhi Wang, Marco Di Renzo, and Arumugam Nallanathan. Robust beamforming design for intelligent reflecting surface aided miso communication systems. *IEEE Wireless Communications Letters*, 9(10):1658–1662, 2020.

- [46] Gui Zhou, Cunhua Pan, Hong Ren, Kezhi Wang, and Arumugam Nallanathan. Intelligent reflecting surface aided multigroup multicast miso communication systems. *IEEE Transactions on Signal Processing*, 68:3236–3251, 2020.